Oxygen vacancy modification of commercial ZnO by hydrogen reduction for the removal of thiabendazole: characterization and kinetic study

Alireza Ranjbari[a,b], Kristof Demeestere[b], Ki-Hyun Kim[c,]**, Philippe M. Heynderickx[a,b,]*

[a] Center for Environmental and Energy Research (CEER) – Engineering of Materials via Catalysis and Characterization, Ghent University Global Campus, 119-5 Songdomunhwa-Ro, Yeonsu-Gu, Incheon, 406-840 South Korea;

[b] Department of Green Chemistry and Technology, Faculty of Bioscience Engineering, Ghent University, 653 Coupure Links, Ghent, B-9000, Belgium;

[c] Department of Civil and Environmental Engineering, Hanyang University, Seoul 04763, Republic of Korea;

** kkim61@hanyang.ac.kr (K.-H. Kim), * Philippe.Heynderickx@Ghent.ac.kr (P. M. Heynderickx)

Abstract

The effect of temperature-programmed H_2 reduction on modification of surface oxygen vacancies in commercial ZnO (C-ZnO) is investigated. The photocatalytic degradation of the fungicide thiabendazole was optimized by treating C-ZnO with 10% H_2/Ar gas at 500°C over 5 hours. The formation of oxygen vacancies and their catalytic activity were compared before and after the reduction treatment based on their characterization analysis (e.g., TPR, FE-SEM, EDS, XPS, Tauc plot, XRD, and BET). Our most recent kinetic modeling was carried out on the experiments using C-ZnO and T500 at different pH values. The highest adsorption removal and photocatalytic degradation rate (and quantum yield) was occurred at pH 3 and 11, respectively. Good reusability of the optimal reduced catalyst was confirmed when tested over five cycles. A strong compatibility between the kinetic modeling results and all characterization analyses supports the potent role of reduction treatment for the modification of oxygen vacancies on photocatalysis.

Keywords

Oxygen vacancy, photocatalysis, ZnO, kinetic modeling, adsorption

1. Introduction

The utility of photocatalysis as a green environmental technology has been continuously increasing over the past decades [1-4]. Semiconductor metal oxides such as zinc oxide are widely used as photocatalysts [5-8]. The advantageous properties of ZnO photocatalysts are well known, and include unique electronic and optical properties, non-toxicity, low cost, and high removal efficiency for various target pollutants [6, 9]. Its application is nonetheless hindered by several limitations, such as a wide bandgap (3.18 to 3.36 eV) for visible light activation [10, 11], high recombination rate of electron-hole pairs, agglomeration, and photocorrosion [12, 13]. To overcome these limitations, enormous efforts have gone into developing various technical options, such as doping with other metals or organic materials, formation of surface defects, metal deposition, heterojunction, and dye sensitization [6, 9, 14].

The formation and/or modification of surface oxygen defects is an effective approach to enhance the photocatalytic activity of a semiconductor catalyst [15, 16]. A surface oxygen vacancy can narrow the bandgap and act as a charge trap as well as an adsorption site in which the photo-induced electron can be conducted to the adsorbate. On the one hand, it can suppress the electron-hole recombination, while on the other hand, it may cause degradation of the adsorbate molecules by charge transfer [17]. Although oxygen vacancies can be produced via various routes, such as doping [18], hydrothermal methods [19], vacuum deoxidation [20], laser deposition [21], and plasma methods [22], the formation of excessive oxygen vacancies may exert a negative effect on the photocatalytic efficiency [23].

Thiabendazole (TBZ) is used as the model compound to explore the efficacy of catalysts selected in this study. This compound is a popular fungicide for products such as fruits, rice, tomatoes, tobacco, and sugar cane. In addition to agricultural use, TBZ has an application for hepatic diseases in livestock [24]. As a result of this broad application in different fields, residual traces of TBZ have been found in various types of media such as agricultural run-off and food industry wastewater effluent [25, 26]. TBZ is an aromatic compound and its residual presence is harmful to the aquatic environment due to its high bio-activity and durability [27]. It is also known for its carcinogenic effect on humans at sufficiently high dosage [28, 29].

The majority of the above-mentioned methods can be used to produce surface oxygen vacancies during the synthesis of the catalysts. This research investigates the possibility of producing an optimal amount of oxygen vacancy through H_2 reduction treatment on an already synthesized catalyst, i.e. commercial ZnO. The optimal reduction temperature and time was studied by using the catalyst for adsorption and photocatalytic removal of TBZ. The formation of oxygen vacancy and its impact on catalyst performance is investigated by different characterization methods (e.g., XPS, XRD, BET, FE-SEM, EDS, and Tauc plot). Furthermore, experiments with sequential adsorption in the dark and photocatalytic degradation under simulated sunlight have been performed at different pH values. The experimental data on both commercial and modified ZnO were kinetically fitted into our recently developed model [30]. The results of this research are expected to offer a broad insight into the role of reduction treatment for the modification of oxygen vacancies on photocatalysis.

2. Materials and methods

2.1. Materials and catalyst synthesis

The reagent grade thiabendazole (CAS: 148-79-8, $C_{10}H_7N_3S$, [201.25 g/mol]) was procured from Sigma-Aldrich. Hydrochloric acid and sodium hydroxide used for pH adjustment, and the commercial ZnO (C-ZnO) selected for oxygen vacancy formation in this study, were also purchased from Sigma-Aldrich. Analytical grade isopropyl alcohol and potassium iodide, used as scavengers, were provided from Daejung company. Catalyst reduction was performed using the catalyst characterizing equipment Autochem II from Micromeritics. Firstly, C-ZnO was pretreated with He at 130°C for 20 minutes. After cooling the catalyst down to 30°C, 10% H_2/Ar was supplied at a flowrate of 60 cm^3/min, then the temperature was gradually raised to the target values of 270, 370, 415, 470, 500, and 650°C at a ramping rate of 10°C/min. These samples were thus named as T270, T370, T415, T470, T500, and T650, respectively. In order to ensure the role of oxygen vacancies in the photocatalytic behavior of the catalysts, some freshly prepared T500 catalyst was immediately treated in a temperature programmed oxidation (TPO) with 5% O_2/Ar at 500°C for 5 hours and the sample was named as TPO-ZnO. To investigate the optimal holding time, the T500 catalyst was held for different times (1, 3, 5, and 7 hrs). To prevent the re-oxidation of the reduced sites, each sample was cooled to room temperature in a He stream after the reduction treatment.

2.2. Photocatalytic experiment

One of the most important points in the preparation of catalysts prior to a photocatalytic process is how to optimize the dispersion of the catalyst [31]. The use of physical dispersion (such as sonication) can drastically increase the surface area of the photocatalyst [32]. However, to have realistic results of the adsorption in the dark-phase experiment, there should be no physical contact between the photocatalyst and the compound in the sonication process [30]. To this end, 25 mg of the catalyst was added to 25 mL of deionized water at the intended initial pH (see Table 1) and sonicated for 30 minutes. The TBZ was added individually in another 25 mL deionized water at the same intended initial pH. Then, the two solutions were mixed (total volume of 50 mL) in a 200 mL beaker and stirred for one hour in the dark. Afterward, the sunlight simulator (Xe lamp DY TECH Co, model DXP 300 (170-410 W)) was switched on at a distance of 10 cm on the top of the reactor to induce photocatalytic degradation (full details in section S.1 of the Supplementary

Information). The light intensity of the Xe lamp was measured as a constant value of 1700±10 W/m^2 for all experiments by a TES 132 solar power meter (Taiwan). To maintain the solution at room temperature, the beaker was placed in a water bath (25±1°C). Samples were taken by a 0.22 μm PES membrane Biofil syringe filter and analyzed by HPLC-PDA, as will be described in section 2.3. The conditions of all performed experiments are summarized in Table 1.

The analyses in presence of isopropyl alcohol (IPA) as hydroxyl radical scavenger with a concentration of 15 mmol L^{-1} and potassium iodide (KI) as hole scavenger with 1.5 mmol L^{-1} were performed at pH 3 and 11 with the same conditions as the above experiments. The scavenger concentrations were selected based on previous studies as the scavenger does not affect the adsorption [33]. The reusability of the modified ZnO was investigated by repeating the process for the optimal reduced catalyst over five cycles (entry 20 of Table 1). The T500 catalyst was separated by 30 minutes' centrifugation at 10,000 rpm. The catalyst was washed with deionized water and dried for 12 hours under vacuum at 100°C. The mass of the reused catalyst was measured and the recovered catalyst was subsequently used in the next experiment. The photolysis of TBZ was investigated in a control experiment at the initial TBZ concentration of 10 mg/L at pH 7 without the presence of the catalyst. Accordingly, there was no considerable change (less than 2% of the initial concentration) in the concentration of TBZ after 6 hours of irradiation, see Figure S.2 in section S.2 of the Supplementary Information.

2.3. Characterization and analytical methods

The temperature-programmed reduction (TPR) analysis of C-ZnO was performed by Micromeritics Autochem II equipment. 200 mg of C-ZnO was pretreated by He at 130°C temperature for 20 minutes and cooled down to 30°C. The gas flow was changed to 10% H_2/Ar and the sample was heated to 650°C with a ramp rate of 10°C/min. The water molecules, formed during reduction, were taken out in a cold trap (kept at temperatures below -80°C). Temperature programmed oxidation (TPO) was performed on the T500 catalyst with the same setup and pretreatment as TPR by using 5% O_2/Ar gas to reoxidize the sample. In addition, pulse chemisorption oxidation (PCO) was used to measure the amount of oxygen vacancies created by H_2 reduction at each temperature. The PCO analysis was immediately performed at the same temperature after reduction of each sample (mass 200 mg) by using 30 cm^3/min Ar gas as carrier and 0.486 cm^3 loop, filled by 5% O_2/Ar for 20 sequential pulses.

The EPR spectra were plotted using Bruker EMX plus equipment at room temperature. The microwave frequency of the X-band spectrometer was 9.64 GHz with a 100 kHz field modulation frequency. The FE-SEM and EDS analyses were performed by a JEOL-7610F PLUS electron microscope. For EDS mapping, the elemental composition of the catalyst was quantified by the identification of 1 million points in the area of about 1 square micrometer. High resolution transmission electron microscope (HR-TEM) analysis was performed on a NEOARM JEM-ARM 200F apparatus. XPS analysis was performed by a Thermo Scientific™ K-Alpha™ XPS system. In order to distinguish the surface oxygen reduction from the bulk oxygen reduction, the first XPS analysis for each sample was performed directly at the surface of the catalyst. Then, the sample was etched with Ar gas for 100 seconds to reach a depth of about 5 nanometers for the second XPS analysis. Powder XRD analysis was performed by Rigaku Ultima IV with a radiation source of Cu (λ=1.54059 Å) at 40 kV and 40 mA, with a 0.02 deg/sec scanning speed. The adsorption-desorption isotherms analysis was performed by ultrapure nitrogen gas at 77.35 K in a Quantachrome Autosorb-iQ 2ST/MP equipment. All samples were degassed for 2 hours under vacuum at 150°C. The surface area of samples was measured by the Brunauer-Emmett-Teller (BET) method, while the pore volumes were calculated by the nonlocal density functional theory

(NLDFT). The FTIR spectrum in the range of 400 to 4000 cm^{-1} of the catalysts, before and after TBZ adsorption, was analyzed by a Thermo Scientific NICOLET iS5. The samples were degassed under vacuum at 120°C for 2 hours prior to the FTIR analysis. The bandgap value of the samples was obtained by the Tauc plot method [34]. The C-ZnO and T500 catalysts with aqueous concentration of 50 mg/L were sonicated for 30 minutes and transferred to a quartz cuvette. The UV-VIS absorption spectrum of the catalysts were analyzed by an Optizen POP spectrophotometer with a wavelength interval of 2 nm. The photoluminescence of the catalysts was analyzed by LabRAM Aramis apparatus provided by Horriba Jovin Yvon company. The spectra were plotted for each catalyst by a He-Cd 325 nm laser in the range of 325 to 900 nm wavelength.

The concentrations of TBZ in water samples were measured by HPLC (Shimadzu LC 2030C) using an ACE 3 AQ column (150×3 mm) and a PDA detector at 300 nm. An isocratic solution of 20 mM ammonium acetate in water and methanol (35/65 v/v) with a flowrate of 0.5 mL/min was used as the mobile phase. The injection volume of the sample in HPLC was 50 µL. The calibration curve of the TBZ concentration is illustrated in section S.3 of the Supplementary Information. The precision of measurement, expressed in terms of RSD based on 8 repetitive runs of 10 mg/L standards, is 3.5%. The values for limit of detection (LOD) and limit of quantification (LOQ) are calculated as 0.33 µmol/L and 1.1 µmol/L, respectively (section S.3 of the Supplementary Information). It should be noted that all of the quantified concentrations of TBZ in this work are above the LOQ.

The LC-MS analysis was performed by Thermofisher ULTIMATE 3000 RSLC with a Q-EXACTIVE ORBITRAP PLUS mass spectrometer. ACQUITY UPLC BEH C18 column with a 0.4 mL/min gradient mobile phase of 0.1% FA in water and 0.1% FA in acetonitrile was used for detecting the degradation products of TBZ. Hanna HI83314 photometer and HI93754A-25 reagent kits were used to measure the COD of the solution by USEPA 410.4 method. TOC was measured by TOC-3300L equipment provided by HUMAS company Korea.

3. Results and Discussion

In order to streamline this section, a brief overview of the work flow is presented. At first, H_2-TPR experiments were performed to evaluate the specific reduction of commercial ZnO. Hereafter, different reduction temperatures could be defined based on the fitted Gaussian peaks in the TPR spectrum with the control of corresponding reduction times. To find the optimal set of reduction time and temperature, the photocatalytic activity of the reduced ZnO samples was experimentally investigated and kinetically modeled by using apparent first-order equations. Physical characterization (TPR, FE-SEM, EDS, XPS, Tauc plot, XRD, and BET) was carried out using both commercial and reduced samples.

The two types of the catalysts representing both the highest activity and the commercial ZnO were tested at different pH values and fitted into the kinetic model which we developed recently [30] to explain the reason for the changes in behavior of the reduced catalyst.

3.1. TPR analysis

To investigate the reduction process of the catalyst, H_2-TPR analysis is performed. Figure 1 illustrates the H_2-TPR profile of ZnO reduction. Several Gaussian peaks were fitted at different temperatures of 270, 370, 415, 470, and 500°C. These peaks represent various oxygen bonds with different strengths on the surface of the catalyst. Therefore, by increasing the reduction temperature, more oxygen vacancies are produced to affect the photocatalytic activity of the catalyst.

3.2. Optimal reduction time and temperature

By considering the reduction peaks in TPR analysis (see Figure 1), photocatalytic activity of reduced ZnO was investigated at different temperatures (T270 to T650°C) and reduction time (1 to 7 hours) in reference to the commercial ZnO (C-ZnO). Adsorption in the dark was performed at the beginning of all experiments for 1 hour. For comparing the total TBZ degradation rate on each catalyst in a simple way, the degradation coefficient (k) of each photocatalytic experiment is estimated by using the first-order kinetics, see Eq (1):

$$C(t) = C_0 \cdot e^{-kt} \tag{1}$$

The initial reaction rate (mol g_{cat}^{-1} h^{-1}) of each catalyst is calculated via Eq (2), where C_0 is the initial concentration of TBZ (mol L^{-1}), k is the degradation coefficient (h^{-1}), V is the volume of the solution (L) and m_{cat} is the mass of catalyst (g L^{-1}).

$$r_0 = \frac{C_0 \cdot k \cdot V}{m_{cat}} \tag{2}$$

As demonstrated in Figure 2a, by increasing the reduction temperature to 500°C, the adsorption removal and initial degradation rate of the commercial ZnO increases from 7.0% and 4.88×10^{-2} (mol g_{cat}^{-1} h^{-1}) to 20.2% and 7.56×10^{-2} (mol g_{cat}^{-1} h^{-1}). Surface oxygen vacancies can act as an adsorption site and a place for transfer of the excitons to adsorbed compound which further results in degradation [35]. However, the further increase of reduction temperature to 650°C causes a significant decrease, specifically in the reaction rate of the catalyst. The reason for such decrease is that in addition to the surface oxygen, the bulk oxygen is also reduced at higher temperatures (see section 3.4). However, the bulk oxygen vacancies cannot be accessible for the adsorption of the contaminants. At the same time, the bulk oxygen vacancies can act as an electron trap but since the excited electrons have no chance to transfer to an adsorbed contaminant molecule, the electron holes will recombine which decreases the efficiency [23].

Figure 2b illustrates the effect of the reduction time on the adsorption and photocatalytic removal of TBZ by modified ZnO. As can be observed, at the optimal reduction temperature of 500°C, the best catalytic activity occurs at a reduction time of 5 hours. Therefore, the optimal reduction temperature and time for the highest adsorption removal and degradation rate of the modified ZnO are found as 500°C and 5 hours, respectively.

3.3. TPO, PCO, and EPR analysis

Temperature programmed oxidation (TPO) analysis was performed to confirm the creation of oxygen vacancies due to the hydrogen reduction treatment. Figure 3a demonstrates the TPO profile of the T500 catalyst. Similar to the TPR analysis, this TPO profile shows 5 different fitted peaks, corresponding to different surface oxygen bond strengths. However, the peaks in TPO profile occur at lower temperatures compared to the peaks of TPR analysis. A possible reason is that the reduction of catalysts requires higher activation energy compared to re-oxidation [36, 37].

Pulse chemisorption oxidation (PCO) was performed to measure the concentration of oxygen vacancies created at each reduction temperature. As illustrated in Figure 3b, the amount of oxygen molecules consumed in PCO analysis rises with an increase in reduction temperature. The number of oxygen molecules consumed at each PCO analysis can be calculated by Eq S.2, explained in section S.4 of the Supplementary Information. Subsequently, the concentration of oxygen vacancies created by H_2 reduction can be estimated by division by the sample mass. Figure 3c illustrates the concentration of oxygen vacancies of each catalyst created by H_2 reduction. As can be observed, by increasing the reduction temperature from 270 to 650°C, the amounts of oxygen vacancies increase from 8.5×10^{-6} to 4.3×10^{-5} mol g_{cat}^{-1}, respectively.

Figure 3d illustrates the electron paramagnetic resonance (EPR) spectra of the C-ZnO and T500 catalysts. As can be observed, both catalysts have the main symmetrical signal at $g = 1.96$. This can be a result of a trapped photo-generated electron on a Zn atom [38, 39]. However, only T500 catalyst has a smaller signal at $g=2.01$ which can be attributed to the presence of oxygen vacancies [40-42].

3.4. FE-SEM, EDS, and HR-TEM analysis

The FE-SEM and EDS images of the C-ZnO and T500 catalysts indicate that reduction of ZnO did not change the particle size and catalyst morphology (Figure 4a to d). The images of FE-SEM and EDS analysis for the other catalysts are illustrated in section S.5 of the Supplementary Information. The results of the EDS analysis are summarized in Table 2. The weight percentage of oxygen at the surface of the catalyst dropped from 24.99% in C-ZnO to 20.84% in T500 and 20.81% in T650. The value of x for the reduced ZnO_{1-x} is estimated based on the atomic percentage of oxygen in the EDS analysis for all samples [43]. This is in agreement with the mass loss of the ZnO sample during the reduction treatment, as shown in Table 2. As the reduction temperature increases from 500 to 650°C, the mass loss of the catalyst considerably increases while the surface oxygen measured by EDS analysis remained almost constant. The reason is that at a high temperature of 650°C, the bulk oxygen rather than the surface oxygen is also reduced which cannot be measured by the EDS analysis. Therefore, to learn more about the changes, XPS analysis was performed at the surface and depth of the catalyst.

In order to further investigate the morphology of the catalysts, HR-TEM analysis was performed on C-ZnO and T500 catalysts. As can be observed in Figure 4e and f, both catalysts demonstrate lattice fringes (d) of about 2.8 Å which corresponds to lattice plane of (100) in ZnO [44]. The insets in Figure 4e and f, illustrate the SAED pattern of the catalysts. The uniform SAED diffraction of both catalysts is a result of the single crystallinity of the nanoparticles. The d-spacing of d = 2.8, 2.6, 2.4, and 1.4 Å corresponding to the lattice planes of (100), (002), (101), and (103) in Figure 4e are in good agreement with ZnO [45].

3.5. XPS analysis

The XPS analysis is performed for all catalysts at the surface and at 5 nm depth. All XPS spectra are adjusted to C 1s at 285 eV. Figure 5a shows the O 1s spectrum with three separate components related to lattice oxygen (O_{lat} at 530 eV), oxygen vacancy (O_{vac} at 531 eV), and adsorbed oxygen (O_{ads} at 532 eV) [46].

Figure 5b illustrates the O_{vac}/O_{lat} ratio for surface and depth XPS of each sample. In line with EDS results, by increasing the reduction temperature to 500°C, the ratio of oxygen vacancy to lattice oxygen at the surface of the catalyst gradually increases from 0.44 to 0.57. However, further increase of reduction temperature to 650°C does not affect the surface O_{vac}/O_{lat} ratio considerably. On the other hand, the ratio of O_{vac}/O_{lat} at depth is almost constant until the reduction temperature of 500°C (about 0.39), while it increases drastically to 0.91 at 650°C.

The electrical conductivity of the samples was investigated by estimating the maximum valence band of the catalysts from the surface XPS spectrum data between -3 and 20 eV. In order to have a systematic procedure for all catalysts, the five-point stencil method was used to fit the tangent line on the XPS spectrum (section S.6 of the Supplementary Information).

Figure 6a illustrates the maximum valence band estimation for both C-ZnO and T500 samples. The rest of samples are shown in section S.6 of the Supplementary Information. Figure 6b compares the maximum valence bands of all samples as determined from both surface and depth XPS spectra. As the reduction temperature rose to 500°C, the maximum valence band of the catalyst experienced an upward shift from 2.43 eV in C-ZnO to 2.62 eV in the T500 catalyst. The higher maximum valence band in T500 indicates a higher oxidative ability of photo-generated electron holes [47]. The electron holes produced by a higher valance band can result into a higher production rate of hydroxyl radicals at basic pH, or direct oxidation of TBZ at the surface of catalyst in acidic conditions [48, 49]. However, a further increase of the reduction temperature to 650°C caused a considerable downward shift in the maximum valence band. The reason for the changes in the maximum valence band is due to changes in the crystalline structure as a result of the reduction treatment and presence of oxygen vacancies [50]. The maximum valence band as determined from the XPS spectra taken at a depth of 5 nm remained constant until the reduction temperature of 500°C. However, it indicated a considerable decrease in the T650 catalyst. This is in agreement with the O 1s depth XPS spectrum of the catalysts in which the O_{vac}/O_{lat} ratio remains constant until the reduction temperature of 500°C. As such, there is no considerable reduction at the bulk oxygen until the reduction temperature of 500°C. Conversely, by increasing the reduction temperature to 650°C, the bulk oxygen can be reduced with a drastic increase in the ratio of O_{vac}/O_{lat}.

3.6. Optical studies by Tauc plot and photoluminescence

The Tauc plot method was used to estimate the bandgap of the catalysts. The absorption spectrum of the aqueous suspensions of the C-ZnO and T500 catalysts are shown in section S.7 of the Supplementary Information. Eq (3) describes the relation between the absorption coefficient (α) and frequency (υ) of the photon irradiated to the aqueous suspension of the catalyst on the one hand and the energy bandgap of the catalyst on the other hand [51]. Where h represents the Planck constant, B is the proportionality constant, and γ represents the electron transition factor with the value of ½ and 2 for direct and indirect transition bandgaps, respectively [34]:

$$(\alpha \times h\nu)^{1/\gamma} = B \cdot (h\nu - E_g) \tag{3}$$

The Tauc plot method was used to study the effect of oxygen vacancies on the energy bandgap of the C-ZnO and T500 catalysts. With the same procedure as for the valence band estimation, the five-point stencil method was used to estimate the energy bandgap from the Tauc plot, see equations (S.3) to (S.5) in section S.6 of the Supplementary Information. Figure 7a illustrates a considerable shift in Tauc plot of T500 relative to C-ZnO. Accordingly, the bandgap of C-ZnO catalyst has dropped from 3.22 to 3.07 eV in the T500 catalyst. The corresponding wavelength of photons that have the minimum energy to activate C-ZnO and T500 are calculated as 385 and 404 nm, respectively (section S.7 of the Supplementary Information). Hence, the modification of oxygen vacancies in the T500 catalyst has increased the photon harvesting toward the visible light [52].

By deducting the band gap of the C-ZnO (3.22 eV) and T500 (3.07 eV) from the maximum valence band of the catalysts estimated from XPS spectra (2.43 eV in C-ZnO and 2.62 eV in T500), conduction band minimum of C-ZnO and T500 can be estimated as -0.79 and -0.45 eV, respectively [53]. Both are more negative than the redox potential of $O_2/O_2^{\circ -}$ (-0.33 eV) [54], resulting in the production of superoxide radicals. The redox potential for OH°/OH^{-} and OH°/H_2O are 1.99 and 2.37 eV, respectively [55]. The maximum valence band of the T500 catalyst (2.62 eV) is sufficiently higher than the redox potential of OH°/OH^{-} and OH°/H_2O, while the one for C-ZnO (2.43 eV) is slightly higher than the redox potential of OH°/H_2O. This can be a possible reason for the lower photocatalytic degradation rate in C-ZnO.

The photoluminescence (PL) spectra for C-ZnO and T500 are illustrated in Figure 7b. The sharp peak at 380 nm in the spectra of C-ZnO is attributed to the electron transition from valence band to the conduction band of ZnO [56]. However, the same peak in T500 catalyst shows a red shift to 421 nm due to the changes in the crystal structure of the reduced catalyst [57]. This is in agreement with the estimated band gap of the catalysts by Tauc plot which is decreased from 3.22 in C-ZnO to 3.07 eV in T500. The wide peak at 663 nm in T500 catalyst is known to represent the presence of oxygen vacancies [58]. These emissions are reported to be a result of electron-hole recombination at the oxygen vacancy sites [59].

3.7. XRD analysis

The XRD spectrum of the T500 catalyst is presented in Figure 8a while those of the C-ZnO and T650 catalysts are in section S.8 of the Supplementary Information. The occurrences of sharp and narrow peaks confirm the high quality and fine particle size with appropriate crystallinity [60]. The three major peaks observed at $2\theta \approx 31.8$, 34.5, and 36.3 can be related to (100), (002), and (101) lattice planes, respectively [61, 62]. The observed lattice planes are in good agreement with standard JCPDS for ZnO [63].

Because of the formation of polycrystalline aggregates, the actual crystalline size of ZnO is smaller than the size of its nano-particles that can be measured by FE-SEM [64]. The oxygen mobility of the catalyst can be investigated by the lattice strain of the crystalline [65]. It can reveal extra information about the changes that occurred in surface oxygen vacancies by H_2 reduction of the catalyst [66]. Therefore, the crystalline size and the lattice strain of the samples are estimated by using Debye-Scherrer [67] and Williamson-Hall equations [60]. Eq (4) represents Scherrer's equation:

$$D = \frac{K\lambda}{\beta \operatorname{Cos}\theta} \tag{4}$$

where D is the crystal size, k (0.9) is the shape factor, λ is the wavelength of radiation of Cuk_α and β is the width of the peak at half of its maximum height.

Table 3 illustrates the average crystalline size of C-ZnO, T500, and T650 samples estimated by Eq (4).

The Williamson-Hall equation used to estimate the crystalline size and lattice strain is shown in Eq (5):

$$\beta \cos\theta = \frac{K\lambda}{D} + 4\varepsilon \sin\theta \qquad (5)$$

where ε is the lattice strain of the sample. A graph of 4sinθ versus β·cosθ is plotted for the first six peaks of the XRD spectrum, which represent the lattice planes of 100, 002, 101, 102, 110, and 103, respectively (see Figure 8b). From the y-axis intercept of the linear fit, the crystalline size (D) can be estimated and the slope of the fit provides the lattice strain ε.

Table 3 illustrates the estimated values for D and ε. With the reduction of C-ZnO to T500 and T650, the lattice strain decreased (lower ε values), which is a measure for oxygen mobility [68]. Hence, it can be concluded that at the higher temperatures of reduction, more oxygen is reduced generating more oxygen vacancies [66]. Furthermore, the lower lattice strain can decrease the free energy of the system, resulting in a higher diffusion of active radicals in the solution while enhancing the efficiency of the reaction [69].

The crystalline size (D) of T650 is higher than those of T500 and C-ZnO for both the Scherrer and Williamson-Hall methods. This can be as a result of exceeding the Tamman-Hüttig temperatures. These temperatures indicate the points that sintering (the process of compacting and combining the crystals of the material without melting) of the catalyst may occur: see Eqs (6) and (7) [70].

$$T_{Huttig} = 0.3 \cdot T_{melting} \qquad (6)$$

$$T_{Tamman} = 0.5 \cdot T_{melting} \qquad (7)$$

For ZnO, these temperatures are 675 and 1124°C, respectively. Since the T650 sample is reduced at temperatures near the Hüttig temperature, it is plausible that the aggregation of crystals has occurred, slightly increasing the crystalline size of the sample [71].

3.8. BET surface area and pore volume

BET surface area and pore volume of C-ZnO, T500, and T650 catalysts were measured by nitrogen adsorption-desorption. Figure 9a demonstrates the adsorption isotherm of the T500 catalyst. The same graphs for C-ZnO and T650 can be found in section S.9 of the Supplementary Information. According to the IUPAC convention, all catalysts are associated with a type-III isotherm that represents slit pores and panel-shaped particles [72, 73]. The BET plot of the adsorption isotherm is illustrated as an inset graph for each catalyst. All BET plots have a linear fitting with R^2 higher than 0.99 ($n \geq 8$).

The method of estimating BET surface area is explained in section S.9 of the Supplementary Information. The BJH pore volume distribution of T500 is demonstrated in Figure 9b while those for the C-ZnO and T650 catalysts are illustrated in section S.9 of the Supplementary Information. Accordingly, all catalysts contain mostly mesopores with pore diameter between 2 and 50 nm [74]. However, by reduction of the C-ZnO at 500°C and 650°C, the quantity of the pores with smaller width has decreased while that of larger pores has increased. This causes an increase in the total pore volume of 8.87×10^{-2} cm^3/g in C-ZnO to 1.06×10^{-1} in T500 and 1.29×10^{-1} cm^3/g in T650, as observed in Figure 9c. This is in agreement with the XPS results that show an increasing ratio of oxygen vacancy to the lattice oxygen at higher reduction temperatures. Furthermore, T650 shows a considerable increase in macropore volume reflecting the bulk oxygen reduction that is also observed in the depth XPS spectrum. The BET surface areas of the catalysts are compared in Figure 9c. By reduction of C-ZnO to T500, the BET surface area increased from 43.0 m^2/g to 48.3

m^2/g. However, by further increase of reduction temperature to T650, the BET surface area drops to 44.3 m^2/g. As described by XRD analysis, due to the reduction near the Hüttig temperature and the subsequent aggregation of crystals, the T650 catalyst has a lower BET surface area. This decrease in BET surface area can be the reason for the observed drop in T650 adsorption removal in the dark (18.8 ± 1.0 %) compared to that of T500 (20.2 ± 0.1%), see Figure 2.

3.9. FTIR and XPS spectra of the adsorbed TBZ

The TBZ adsorption on the surface of the catalyst was verified by FTIR analysis. Figure 10a illustrates the FTIR spectra of CZnO, T500, and T500 after adsorption of TBZ for one hour in the dark. Comparing the graph of CZnO and T500 catalyst, a strong peak has occurred at 983 cm^{-1} in the FTIR spectra of T500 that are related to vibrational frequencies due to the structural changes after hydrogen reduction [57]. Several peaks at the FTIR spectra of T500 after TBZ adsorption clearly indicate the presence of TBZ adsorbates. The first peak at 729 cm^{-1} is referred to C-S bond in TBZ structure [75]. The peaks at 1248 and 1406 cm^{-1} are attributed to the stretching of C-H bond and C-C elongation, respectively [76]. In addition, the peak at 1310 cm^{-1} indicates stretching vibration of C-N bond in the adsorbed TBZ molecule [77]. The further peaks at 2780 and 3043 cm^{-1} are related to $C-H_2$ and N-H stretching, respectively [78].

Figure 10b demonstrates the XPS spectra of T500, before and after TBZ adsorption. As can be observed, a small peak at 399 eV (N 1s) has emerged in the XPS spectra of T500 after the TBZ adsorption. This peak can be assigned to N-C bonding in TBZ adsorbate [79]. Figure S.11a and b in section S.10 of the Supplementary Information illustrates the C 1s spectrum of T500 before and after TBZ adsorption. The mentioned spectrum of fresh T500 contains only one peak at 284.6 eV which corresponds to C-C or C=C bonds in the carbon tape [80]. After TBZ adsorption, an additional peak was observed at 286.4 eV that can be attributed to the C=N bonding of the adsorbed TBZ [79].

The atomic percentage of nitrogen and carbon calculated by XPS spectra increased from 0.0 and 2.5% in fresh T500 to 0.9 and 5.1% in T500 after TBZ adsorption, respectively. While the atomic percentage of zinc has remained almost constant (44.4 in fresh T500 and 44.1 in T500 after TBZ adsorption) and the oxygen percentage decreased from 53.1% in fresh T500 to 49.9% in T500 with TBZ adsorbate. A possible reason is that the adsorption sites for TBZ adsorbates were mostly oxygen vacancies.

3.10. Kinetic modeling and the effect of pH

To have a better insight into the effects of oxygen vacancy modification on the behavior of the C-ZnO, T500, and TPO-ZnO catalysts, the experimental results are evaluated at different pH values by our recently published kinetic model [30], as given by Eqs (8) to (11). This model simultaneously considers reversible adsorption and photocatalytic degradation by active radicals in the solution as well as degradation on the catalyst surface (via holes):

$$V\frac{dC_{aq}}{dt} = -V\sum_{i=0}^{2}(k_{1,i}\alpha_i C_{aq}C_* - k_{2,i}C_{i,ad}) - Vk_3C_{aq}\xi \tag{8}$$

$$m_{cat}\frac{dC_{ad}}{dt} = +V\sum_{i=0}^{2}(k_{1,i}\alpha_i C_{aq}C_* - k_{2,i}C_{i,ad}) - m_{cat}k_4C_{ad}\xi \tag{9}$$

$$C_* + m\sum_{i=0}^{2}C_{i,ad} = C_{tot} \tag{10}$$

$$\begin{cases} \xi = 0 \quad , \quad t < t^* \\ \xi = 1 \quad , \quad t^* \le t \end{cases} \tag{11}$$

Eq (8) defines the changes in aqueous concentration of TBZ as the adsorption and desorption take place together with photocatalytic degradation by active radicals in the solution. Eq (9) describes the changes of TBZ adsorbate concentration on the catalyst surface by considering the reversible adsorption-desorption and photocatalytic degradation of adsorbates on the catalyst surface by electron holes. The symbols V, m_{cat}, C_{aq}, and C_{ad} in Eqs. (8) and (9) represent the volume (L) of the solution, catalyst mass (g), liquid phase concentration (mol L^{-1}), and adsorbed TBZ concentration per mass of catalyst (mol g^{-1}), respectively.

In order to address the pH impact in Eqs (8) to (11), the dissociation of TBZ was considered in the kinetic model. The free electron pair of the nitrogen at the central ring of the TBZ (see Figure 11) can accept a proton at enough low pH values, which results in a positive charge on TBZ. On the other hand, at sufficiently alkaline conditions, the hydrogen attached to the nitrogen of the inner ring could be separated from the TBZ molecule giving it a negative charge. The acid dissociation constants have been taken into account, as estimated in our previous work. The $pK_{a,1}$ and $pK_{a,2}$ for positive and negative species of TBZ are equal to 5.09 and 7.96, respectively [30]. Accordingly, α_0 to α_2, in Eqs (S.9) to (S.11) in section S.11 of the Supplementary Information, can be used to express the partition ratio of positive, neutral, and negative species of TBZ, respectively.

$k_{1,i}$ is are the adsorption coefficient and $k_{2,i}$ is the desorption coefficient for each TBZ specimen (i). Parameter k_3 defines the degradation coefficient of the aqueous TBZ caused by reactive radicals in the solution. Parameter k_4 corresponds to the degradation coefficient of the adsorbate TBZ by electron-holes at the photocatalyst surface. Parameters k_3 and k_4 are assumed to be constant in every different TBZ species due to a non-selective reactivity of radicals and electron-holes at a specific pH.

Eq (10) defines the site balance on the catalyst surface, where C_* and C_{ad} represent the free and occupied active sites on the catalyst surface, respectively. Parameter m represents the average number of active sites covered by one molecule of adsorbed TBZ [30]. The light conditions for

Eqs (8) to (10) are shown in Eq (11) with ξ as light switch. For the first 60 minutes (t^*) in the dark phase of the experiment, the second terms of Eqs (8) and (9) are zero (ξ =0), while the TBZ removal is only by adsorption. Thereafter, the lights are switched on to activate the photocatalytic degradation of TBZ in both continuity equations (CEs) of (8) and (9) (ξ =1).

The numerical integration of CEs for every 1 minute time step was performed by an in-house code using Excel® software. The initial conditions of $C_{aq(t=0)} = C_0$ and $C_{ad(t=0)} = 0$ were considered for the start of numerical integration. Kinetic parameters were estimated based on a GRG nonlinear solving method by minimizing the residual sum of squares as expressed by Eq (12). N_j is the total samples for each experiment while n is the number total experiments in the modeling as described in Table 1:

$$S = \sum_{i=1}^{n} \sum_{j=1}^{N_j} (C_{aq,i,j} - \hat{C}_{aq,i,j})^2 \quad \rightarrow \quad \min \tag{12}$$

3.10.1. Modeling results

Continuous adsorption and photocatalytic degradation of TBZ was performed at different pHs with C-ZnO, T500, and TPO-ZnO catalysts. The dots in Figure 12a to c represent the experimental data of TBZ removal by the catalysts at the initial pH values of 3, 7, and 11. The same graphs for the initial pHs of 5 and 9 are provided in section S.11 of the Supplementary Information, along with the graphs comparing all experiments at different pHs. Accordingly, the T500 catalyst has higher adsorption removal and degradation rate than other catalysts at all pHs. While, the TPO-ZnO catalyst has the lowest adsorption among all the catalysts. The TBZ removal by adsorption in the dark drops considerably with increasing pH, regardless of reduction treatment. In contrast, the overall degradation rate (considering the total degradation in the liquid and the surface of the catalyst) for all catalysts rises significantly at alkaline pH conditions.

Continuous lines in Figure 12 indicates the calculated data by the kinetic model. Table 4 shows the values of the estimated parameters by the model. Each TBZ specimen has a constant $k_{1,i}$ and $k_{2,i}$ at all pHs, while k_3 and k_4 have specified values at each pH. The total concentration values of active sites (C_{tot}) in C-ZnO and T500 indicate an increase of about 68% from 1.17 10^{-4} to 1.96 10^{-4} mol g^{-1} after reduction treatment. However, the estimated amount of active sites in TPO-ZnO catalyst has decreased to 1.06 10^{-4} mol g^{-1}. As such, it is experimentally confirmed that more oxygen vacancies are produced at the surface of the T500 catalyst by H_2 reduction [81, 82]. While the re-oxidation of the T500 catalyst at 500°C reduced the amount of oxygen vacancies in TPO-ZnO to even lower values than that of C-ZnO. The possible reason can be that C-ZnO has initially some oxygen vacancies before the H_2 reduction. During the oxidation of the TPO-ZnO at 500°C, not only the oxygen vacancies produced by H_2 reduction, but also the initial oxygen vacancies of C-ZnO can be re-oxidized. Figure S.14 in section S.11 of the Supplementary Information illustrates the results of the PCO analysis for the C-ZnO and T500 catalysts at 500°C. As observed, the oxygen vacancy concentration of C-ZnO catalyst that can be oxidized at 500°C is 1.33 10^{-5} mol g_{cat}^{-1}, while the value for T500 catalyst is 3.99 10^{-5} mol g_{cat}^{-1}. The XPS O 1s spectrum of TPO-ZnO is shown in Figure S.15 of the Supplementary Information. As can be observed, the oxygen vacancy (O_{vac}) peak at 531 eV is considerably smaller than that of C-ZnO, resulting in a remarkable drop of O_{vac}/O_{lat} ratio from 0.44 in C-ZnO to 0.31 in TPO-ZnO. The reduced amount of oxygen vacancies in TPO-ZnO sample can be a possible reason for its lower performance in adsorption removal and photocatalytic degradation of TBZ.

The value for m has increased from 1.12 in C-ZnO to 2.09 in T500. This is due to a smaller increase in the BET surface area of the catalyst after H_2 reduction (about 12%, from 43.0 to 48.3 m^2/g), while there was a significant increase in total active sites (about 68%, from 1.17 10^{-4} to 1.96

10^{-4} mol.g^{-1}). Thereby, the active sites for the T500 catalyst are more tightly placed on the surface of the catalyst. On the other hand, as the surface area of the TBZ molecule remained constant, it can yield a higher m value by retaining more active sites. To confirm this, the average surface area values for each active site on C-ZnO and T500 are calculated as 61 Å^2 and 41 Å^2, respectively, when the BET surface area is divided by the amount of C_{tot} for each catalyst. Note that the TBZ surface area is reported as about 82 Å^2 [83]. Hence, the estimated values for m are in agreement with the ratio of TBZ to the active site area of the catalysts.

As the initial pH increases from 3 to 11, the extent of TBZ removal by C-ZnO, T500, and TPO-ZnO in the dark (adsorption) drops from 12.2% to 6.6%, from 26.3% to 15.2%, and from 9.2% to 5.0%, respectively. As shown in Figure 11, positive and negative species of TBZ are dominant at acidic and alkaline conditions, respectively. The adsorption equilibrium coefficient $K_{ad,i}$ can be calculated for each TBZ species by dividing the estimated k_1 and k_2 parameters denoted as the adsorption and desorption coefficient, respectively (see Table 4). K_{ad} indicates a significant decrease by going from positive to neutral and negative species for C-ZnO (from 1.49 10^4 to 1.33 10^3 L mol^{-1}), T500 (from 2.39 10^4 to 2.18 10^3 L mol^{-1}), and TPO-ZnO (from 1.40 10^4 to 1.04 10^3 L mol^{-1}) catalysts. This may be accounted for by the occurrence of a negative zeta potential of the ZnO catalyst in aqueous solutions [84, 85] which was confirmed by comparing the point of zero charge (PZC) for C-ZnO and T500 catalysts (see Figure S.16 in the section S.11 of the Supplementary Information). As both C-ZnO and T500 in initial acidic conditions tend to adsorb positive protons in the solution, a considerable increase is observed in the solution pH. At basic pH conditions, the pH of the solution drops slightly as C-ZnO adsorbs hydroxyl anions. The pH values still increased up to 10 as the T500 continued to adsorb protons. Thereby, the PZC of C-ZnO has been shifted from pH 7.5 to about 10 in the T500 catalyst. This indicates a more negative zeta potential in T500 with an enhanced adsorption removal of TBZ compared to C-ZnO. Furthermore, it can thus explain the higher adsorption removal of TBZ in acidic conditions compared to basic pHs in both catalysts.

Figure 12d illustrates the changes in k_3 and k_4 as a function of solution pH. The X axis of this figure is based on the solution pH after the catalysts were mixed with the initial solution. The k_3 values rise with the increase of the pH for all catalysts. However, k_3 has higher values for the T500 catalyst at all pHs. The parameter k_3 represents the degradation of TBZ by active radicals in the solution. By increasing the pH of the solution, the amount of hydroxyl anions significantly increases to stimulate the production rate of hydroxyl radicals by the catalysts [86, 87]. On the other hand, k_4 defines the degradation of TBZ adsorbates by the photo generated electron-holes on the ZnO surface. The value of k_4 reaches its maximum at pH 3 for all catalysts. By increasing the pH toward alkaline conditions, the estimated values for k_4 show a significant drop. This can be a result of low adsorption in alkaline pH. In addition, at low concentrations of hydroxyl anions (acidic pH values), electron holes can facilitate the degradation of TBZ through the direct reaction with adsorbates [88]. As more oxygen vacancies are generated by the reduction of C-ZnO, higher adsorption/degradation at the surface of the catalyst, accompanied by the increasing number of active sites, can cause a significant rise in values for k_4 at T500.

3.10.2. Methylene blue degradation

In order to confirm the superiority of T500 catalyst over C-ZnO, adsorption removal and photocatalytic degradation were performed on a typical model molecule in many studies, namely methylene blue (MB). Figure S.17 in section S.11 of the Supplementary Information demonstrates the effect of pH on adsorption removal and initial reaction rate calculated by Eq. (2). As observed, at all pHs, T500 displays higher adsorption (dark zone adsorption equilibrium) and degradation rate (light zone), compared to C-ZnO. By decreasing the pH from 11 to 3, adsorption removal increases from 11.7 to 23.8% in T500 and from 8.2 to 18.6% in C-ZnO. The initial reaction rate of T500 drastically increases from 0.19 at pH 3 to 1.07 mol kg_{cat}^{-1} hr^{-1} at pH 11 (factor ~5.6), while the values for C-ZnO increase from 0.14 at pH 3 to 0.69 mol kg_{cat}^{-1} hr^{-1} at pH 11 (factor ~4.9).

3.10.3. Effect of scavengers

To further investigate the effect of pH on the parameters k_3 and k_4, extra experiments were performed by T500 catalyst at pH 3 and 11 in presence of hydroxyl radical scavengers (IPA) and hole scavengers (KI). Figure 13a and b illustrate the experimental and calculated data (using the proposed kinetic model) with scavengers at pH 3 and 11. As can be observed, the presence of scavengers has not affected the adsorption in dark. Hence, the parameters k_1, k_2, C_{tot}, and m have remained constant and the curves were fitted by estimation of parameters k_3 and k_4 for each of the scavenger experiments. At pH 11, the photocatalytic degradation rate decreased significantly in presence of hydroxyl radical scavengers, while the existence of hole scavengers did not considerably affect the degradation rate. On the other hand, the effect of hole scavengers is more pronounced than hydroxyl radical scavenger effect at pH 3. This is in agreement with the results of the parameter estimation by the model that shows higher k_3 values at basic conditions while indicating higher k_4 values at acidic conditions. Figure 13c compares the estimated k_3 and k_4 in photocatalytic experiments by T500 catalyst with and without scavengers. In presence of hydroxyl radical scavengers, k_3 decreases significantly from 9.23 10^{-2} to 6.94 10^{-3} at pH 11 (factor ~13.3) and from 2.34 10^{-2} to 2.67 10^{-3} at pH 3 (factor ~8.8). By addition of the hole scavenger, the k_4 values drop from 5.90 10^{-2} to 1.67 10^{-3} at pH 3 (factor ~35.3) and at pH 11, remarkably the value of 3.66 10^{-3} is completely reduced to 0.00.

As liquid degradation reactions are bimolecular in nature, the concentration of radicals and holes was tacitly taken up in the reaction coefficients k_3 and k_4. As such, the third term of the right hand side of Eqs (8) and (9) can be described in terms of hydroxyl radical and hole concentration as Eqs (13) and (14).

$$k_3 C_{aq} = k_3^{\circ} C_{OH^{\circ}} C_{aq} \rightarrow k_3 = k_3^{\circ} C_{OH^{\circ}} \tag{13}$$

$$k_4 C_{ad} = k_4^{\circ} C_{h^+} C_{ad} \rightarrow k_4 = k_4^{\circ} C_{h^+} \tag{14}$$

Where C_{OH}° and C_h^+ are the hydroxyl radicals and electron holes concentrations. The k°_3 and k°_4 represent the bimolecular degradation rate coefficient by radicals and electron holes that are considered to be constant regardless of experimental conditions. In the same way, k'_3 and k'_4 which are the estimated parameters in presence of hydroxyl radical and hole scavengers, can be defined as Eqs (15) and (16).

$$k_3^{'} = k_3^{\circ} C_{OH^{\circ}}^{'} \tag{15}$$

$$k_4^{'} = k_4^{\circ} C_{h^+}^{'} \tag{16}$$

With $C'_{OH}{}^{\circ}$ and $C'_h{}^+$ the concentration of hydroxyl radicals and electron-holes in the presence of scavengers. Hence, the relative hydroxyl radical and electron-hole concentrations after adding the scavengers can be calculated with Eqs (17) and (18).

$$\frac{k_3^{'}}{k_3} = \frac{C_{OH^{\circ}}^{'}}{C_{OH^{\circ}}} \tag{17}$$

$$\frac{k_4^{'}}{k_4} = \frac{C_{h^+}^{'}}{C_{h^+}} \tag{18}$$

By using Eqs (17) and (18), the decrease in hydroxyl radicals after adding the scavengers is 89 and 92% at pH 3 and 11, respectively. The decrease in electron-holes concentration in presence of electron-hole scavengers is 97% at pH 3 and 100% at pH 11.

The presented results indicate the practicality of the proposed model in describing the kinetic parameters for the simultaneous degradation reactions at the catalyst surface by electron-holes and in the solution by active radicals and from their ratio (without and with scavenger) useful quantitative information is obtained regarding the scavengers effect.

3.10.4. Reaction mechanism

Based on the developed kinetic model and all aforementioned observations, the following reaction mechanism in Figure 14 is suggested for the photocatalytic degradation of TBZ by oxygen vacancy modified ZnO. The light induced electron-holes in conduction band and valence band can react with oxygen or hydroxyl anions in the solution and generate reactive radicals as described in Eqs (19) and (20) [89, 90].

$$OH^- + h_{VB}^+ \rightarrow HO^\circ \tag{19}$$

$$O_2 + e_{CB}^- \rightarrow O_2^{\circ-} \tag{20}$$

Subsequently, the generated radicals attack the aqueous TBZ molecules in the solution and cause degradation (defined by k_3 in the model). On the other hand, the adsorbed TBZ molecules at the catalyst surface, especially at acidic pH conditions where the concentration of hydroxyl anions is low, can directly react with the photo-induced electron-holes and they decompose into smaller molecules [91]. The role of surface oxygen vacancies is to act as an adsorption site and improve the electron transfer efficiency to the adsorbates. In this way, they prevent electron-hole recombination and facilitate the degradation process. Contrastingly in the case of bulk oxygen vacancies, they can attract the photo-induced electron, but there is no adsorbed molecule to transfer the electron [35, 92]. Hence, the trapped electrons in the bulk oxygen vacancy have no other way rather than recombining with the holes. Overall, the bulk oxygen vacancies may act like a short circuit and suppress photocatalytic degradation by causing electron-hole recombination [93].

3.11. Degradation pathway and mineralization

To find the possible products of TBZ degradation, liquid chromatography combined with mass spectroscopy (LC-MS) was performed on samples of the photocatalytic experiment with T500 catalyst and an initial TBZ concentration of 20 mg/L. Several intermediates were detected in the chromatogram of the analysis. Figure 15 illustrates four possible degradation pathways proposed based on the detected compounds. The first pathway considers the C-C bond cleavage between the second and third TBZ rings and the subsequent opening of the second ring by a hydroxyl radical attack [94, 95]. Pathway 2 is as a result of direct radical attack on thiazole (ring 3) and opening the ring followed by a ring 2 opening [95]. In the third pathway, multiple hydroxyl radicals attack the first ring of TBZ and this results in a ring 1 opening degradation [24]. The last pathway is suggested by the direct ring opening of the imidazole ring (ring 2), followed by thiazole ring opening [96].

TOC and COD analyses were performed to compare the performance of C-ZnO and T500 catalysts in terms of TBZ mineralization. Figure S.18 in section S.12 of the Supplementary Information demonstrates the COD and TOC removal after 1 hour of adsorption and 3 hours of photocatalytic degradation at pH 7. COD removal by adsorption has increased from 9.4 in C-ZnO to 17.9% in T500. Similarly, the results of TOC removal by adsorption show a considerable increase from 11.5 in C-ZnO to 25.6% in T500. Further photocatalytic degradation for 3 hours under simulated sunlight increases the COD removal to 77.4 and 87.5% by C-ZnO and T500, respectively. The measured TOC removal after the same duration of photocatalytic degradation reaches 78.0 and 85.7% in presence of C-ZnO and T500, respectively.

3.12. Performance evaluation based on quantum yield

It was found that all ZnO catalysts can achieve a total removal of TBZ by more than 98% regardless of reduction treatment. Nonetheless, the T500 catalyst outperformed in that it can proceed in a considerably shorter reaction time. The $t_{50}$and t_{90} of the C-ZnO and T500 catalysts, representing the reaction time for 50% and 90% of TBZ removal, are shown in Figures S.19 a and b in section S.13 of the Supplementary Information. The T500 catalyst has lower $t_{1/2}$ and t_{90} at all pHs which indicate a considerably higher degradation rate (e.g., relative to C-ZnO). As the pH is raised from 3 to 11, $t_{1/2}$ for C-ZnO and T500 drops from 44 to 21 and from 21 to 9 minutes, respectively. The t_{90} also decreases from 146 to 68 minutes in C-ZnO and from 66 to 30 minutes in T500 when the pH is changed from 3 to 11. As such, a higher degradation rate is achieved at basic conditions.

In order to evaluate the energy efficiency of the catalysts, the quantum yield values for both C-ZnO and T500 catalysts have been calculated at different pH values. Quantum yield (QY) is described as the proportion of degraded TBZ molecules to the amount of photons entering the liquid per unit of time [97]. In this study, in order to have a similar approach in all experiments, the t_{90} reaction time is used for the calculation of the quantum yield. Further explanation on the calculation of QY is provided in section S.13 of the Supplementary Information. Figure S.19c compares the QY for C-ZnO and T500 at different initial pH. As can be observed, the T500 catalyst has a significantly higher value of QY at all pH values. This may reflect its higher degradation rate due to the introduction of surface oxygen vacancies at the T500 catalyst by hydrogen reduction. In addition, T500 has a narrower band gap which allows it to absorb a broader range of photons with larger wavelengths. The QY for C-ZnO and T500, when computed at initial pH of 3, is about 1.17 10^{-5} and 2.15 10^{-5} molecules photon^{-1}, respectively. Due to the increase of degradation rate and a significant decrease in the required degradation time at basic conditions, the maximum QY values of the catalysts at initial pH of 11 reaches 2.64 10^{-5} and 5.45 10^{-5} molecules photon^{-1}, respectively.

To consider the effect of the catalyst dose on QY, the space time yield (STY) was calculated for both catalysts [97]. STY is described as the value of QY per the unit mass of the used catalyst in the process (see section S.13 of the Supplementary Information). The minimum STY calculated at an initial pH of 3 for C-ZnO and T500 were about 4.69 10^{-7} and 8.60 10^{-7} molecules photon^{-1} $\text{mg}_{\text{cat}}^{-1}$, respectively. By increasing the initial pH values to 11, the STY of the catalysts rises to 1.06 10^{-6} and 2.18 10^{-6} molecules photon^{-1} $\text{mg}_{\text{cat}}^{-1}$, respectively.

The reported values of QY and STY in the literature for photocatalytic degradation of methylene blue are 6.7×10^{-8} to 3.8×10^{-6} molecules per photon and 2.8×10^{-10} to 1.0×10^{-7} molecules per photon per mg_{cat}, respectively [97]. Accordingly, T500 is found to be noticeably superior over other reported systems in terms of the key performance metrics like QY and STY.

3.13. Reusability

One of the most important aspects of photocatalysis is the possibility of reusing the catalyst [98]. Five batches of sequential experiments were carried out at pH 7 in order to evaluate the reusability of T500 with the optimal surface oxygen vacancy. Figure S.20 in section S.14 of the Supplementary Information illustrates the adsorption in the dark and total removal of TBZ in each cycle. No considerable change has been observed in catalytic activity after 5 cycles of TBZ degradation. The adsorption (in dark) and total (dark and light phases) removal of TBZ in all cycles are about 20.3 ± 1.3 % and 98.1 ± 0.6 %, respectively.

In order to investigate the possible changes in the structure or surface oxygen vacancy of the T500 catalyst, XPS, FE-SEM, EDS, TEM, PCO, and EPR analyses were performed on the catalyst after 5 cycles of reuse. Figure S.21 in section S.14 of the Supplementary Information illustrates the O 1s spectrum of the XPS data for the 5-times-reused T500 at the surface and depth of about 5 nm of the catalyst. The oxygen vacancy to lattice oxygen ratio of the reused catalyst at the surface is about 55.4 %, which is almost the same as for the fresh T500 (56.9 %). The same ratio for the depth spectra of reused catalyst is 39.4 %, while that for fresh T500 is about 38.6 %. Figure S.22 in section S.14 of the Supplementary Information shows the FE-SEM, EDS, and TEM images of the reused catalyst. The particle size and shapes are the same as for the fresh T500 catalyst. EDS results show that the weight percentage of oxygen atoms at the surface is about 20.91 %, which is almost the same as for the fresh T500 catalyst (20.80%), as seen in Table 2. The TEM image shows that the d-spacing of the reused T500 catalyst is about 2.82 Å which corresponds to the lattice plain of (100). The same as the fresh T500 catalyst, the SAED pattern illustrates the lattice plains of (100), (002), (101), and (103) that are in agreement with the results of XRD analysis for T500 catalyst.

Figure S.23a in section S.14 of the Supplementary Information shows the EPR analysis of the reused T500 catalyst. Similar to the fresh T500 EPR graph, the reused catalyst has two signals at g = 1.96 and 2.01 that are attributed to Zn and oxygen vacancies, respectively. Figure S.21b illustrates the PCO analysis of reused T500 catalyst compared to the fresh T500. The results indicate that the concentration of oxygen vacancies is almost equal in both reused (3.97×10^{-5} mol g_{cat}^{-1}) and fresh catalyst (3.99×10^{-5} mol g_{cat}^{-1}). This provides experimental proof that the oxygen vacancies remained stable during the photocatalytic process.

The reason for the oxygen vacancy stability is that most of the H_2 reduction occurred at high temperatures, see TPR graph in Figure 1. Hence, reoxidation of the catalyst needs a high amount of energy which is not provided at room temperature [37]. This can be confirmed by the TPO results on the T500 catalyst in Figure 3a, which shows that the most of reoxidation occurs at temperatures higher than 100°C. To further investigate the possibility of reoxidation of oxygen vacancies, PCO analysis was performed on fresh T500 catalyst at room temperature. As indicated in Figure S.23b in section S.14 of the Supplementary Information, no oxygen consumption was observed in PCO analysis at room temperature. However, a very slow rate of oxygen vacancy reoxidation in air at room temperature is reported in some studies [42, 99]. To prevent eventual reoxidation at room temperature conditions, the catalyst was stored in closed tubes, and flushed with N_2 to minimize its contact with atmospheric oxygen. Furthermore, it is reported that the UVA beams available in the solution during the photocatalytic process by simulated sunlight together with annealing under vacuum at 100°C (which is performed for drying the catalyst after each reuse cycle) can prevent the reoxidation of the vacancies [100]. Hence, it can be concluded that no considerable changes have occurred in the oxygen vacancy of the catalyst after 5 reuse cycles.

Closing this section, it is worthwhile to compare the photocatalytic performance of the present work and some of the similar studies that have been recently published. The apparent first order reaction rate of the reported studies is illustrated in Table 5. However, the proposed kinetic model in the present work has two separate degradation rate coefficients k_3 and k_4 (for degradation in the solution and on the catalyst surface) that should be considered at the same time. By taking the sum of k_3 and k_4, the T500 catalyst displays the highest photocatalytic activity amongst similar published works.

4. Conclusions

The oxygen vacancy has a considerable effect on both the adsorption capacity and photocatalytic behavior of commercial ZnO catalysts. The C-ZnO catalyst attained the optimal amount of surface oxygen vacancies when subject to a reduction treatment at 500 °C for 5 hours. As such, it exhibited pronouncedly improved performances such as increases in the TBZ adsorption removal (e.g., from 7.0% to 20.2%) and initial reaction rate (e.g., from 4.88 10^{-2} to 7.56 10^{-2} (mol g-cat^{-1} hr^{-1})).

Characterization of the commercial and reduced catalysts by different techniques such as XPS, XRD, BET, FE-SEM, EDS, Tauc plot, TEM, EPR, TPO, PCO, PL, and FTIR have confirmed the relation between surface oxygen vacancies and the activity of the catalysts. EPR, PL, TPO, and PCO analyses indicate the creation of oxygen vacancies due to hydrogen reduction. XPS analysis shows an increase in oxygen vacancy to lattice oxygen ratio, while XRD analysis confirms the decrease of oxygen mobility in reduced catalysts. Tauc plot analysis indicates a narrower bandgap for the reduced catalyst. This narrowed bandgap can increase the amount of photons in the range of visible light, absorbed by the catalyst. An upward shift was also observed in the maximum valence band of the reduced catalyst (T500), indicating a higher production rate of hydroxyl radicals at basic pH as well as a higher degradation rate at the surface of the catalyst at acidic conditions. Such superior performance of T500 catalyst is also in line with the estimated quantum yield patterns between different catalysts. FTIR and XPS analyses on T500 catalyst after TBZ adsorption in the dark confirmed the presence of TBZ molecules at the surface of the catalyst.

Both C-ZnO and T500 have higher adsorption removal at acidic pH and higher degradation removal at basic pHs. Based on the kinetic model we developed recently, it was possible to offer valuable insights into continuous adsorption/degradation at distinct pH values. The total amount of active sites increased from 1.17 10^{-4} in C-ZnO to 1.96 10^{-4} mol g^{-1} in T500. However, the value for the parameter m increased from 1.12 to 2.09, which shows that the active sites are more concentrated and closer to each other. Due to the negative zeta potential of both C-ZnO and T500, positive specimens of TBZ have a superior adsorption rate coefficient with a smaller desorption rate coefficient than the neutral and negative species. The parameters k_3 and k_4, which represent the degradation rate coefficient inside the liquid and at the catalyst surface, have linear relationships with pH such that k_3 increases with increasing pH while k_4 is higher at acidic pH. This reveals that under basic conditions, most degradation occurs in the solution, while most of that occurs on the surface of the catalyst at acidic conditions, which was approved by experiments performed in presence of hydroxyl radical and hole scavengers. In C-ZnO, as the adsorption removal is very low, the k_4 values are sufficiently small to be neglected. Accordingly, it can be concluded that almost all of the degradation is due to active radicals in the solution. The degradation pathway of TBZ was investigated by LC-MS analysis, indicating that almost complete mineralization can be achieved. The COD and TOC removal of TBZ degradation by T500 reached 87.5 and 85.7%, respectively. The reusability of T500 catalyst has been confirmed up to five sequential cycles as supported by XPS, FE-SEM, EDS, TEM, EPR, and PCO analyses. The results of this study indicate that a considerable improvement in photocatalytic activity of commercial catalysts can be obtained by performing surface oxygen reduction treatments.

Acknowledgements

The authors acknowledge the Research and Development Program of Ghent University Global Campus (GUGC), Korea. KHK acknowledges support made by a grant from the National Research Foundation of Korea (NRF) funded by the Ministry of Science and ITC (MSIT) of Korean government (Grant No: 2021R1A3B1068304). The authors thank Prof. Jonathan Ozelton from the

Center for Language and Learning (LLC) at Ghent University Global Campus (GUGC) for proofreading of the document. The authors thank Jihee Yu, Ju Ho Kim and Jiyun Kim for participating in photocatalytic experiments with methylene blue. The authors would like to thank the reviewers for the constructive remarks.

List of Symbols

Roman symbols

C	Concentration of total species of thiabendazole	mol L^{-1}
C_*	Concentration of available active sites on catalyst surface	mol g^{-1}
C_{tot}	Concentration of total active sites on catalyst surface	mol g^{-1}
k_1	Adsorption rate coefficient	g mol^{-1} min^{-1}
k_2	Desorption rate coefficient	g L^{-1} min^{-1}
k_3	Degradation rate coefficient by active radicals in solution	min^{-1}
k_4	Degradation rate coefficient by electron holes at catalyst surface	min^{-1}
K_{ad}	Adsorption coefficient	L mol^{-1}
K_a	Acid dissociation constant	mol L^{-1}
m	Occupied active sites to adsorbed thiabendazole molecules ratio	mol mol^{-1}
m_{cat}	Catalyst mass	g
n	Number of each experiment	-
N_j	Number of samples at different retention times in an experiment	-
S	Residual sum of squares	mol^2 L^{-2}
t_{50}	Reaction time for 50% TBZ removal	-
t_{90}	Reaction time for 90% TBZ removal	-
V	Volume of the solution	L

Greek symbols

α_i	Partition ratio of species i	mol mol^{-1}
ξ	Light switch (= 0 for the dark zone; = 1 for the light zone, see Eq (11))	-

Subscripts

ad	Adsorbed
aq	Aqueous
i	Specimen of thiabendazole
exp	Experimental data
^	Calculated value

Abbreviations and acronyms

A^-	Negative thiabendazole specimen	
AH	Neutral thiabendazole molecule	
AH_2^+	Positive thiabendazole specimen	
A_T	Total thiabendazole specimen	
BET	Brunauer-Emmett-Teller	
BJH	Barrett-Joyner-Halenda	
CE	Continuity equation	
C-ZnO	Commercial zinc oxide	
EPR	Electron paramagnetic resonance	
LI	Light intensity	$W\ m^{-2}$
LOD	Limit of detection	$mg\ L^{-1}$ or $mol\ L^{-1}$
LOQ	Limit of quantification	$mg\ L^{-1}$ or $mol\ L^{-1}$
PCO	Pulse chemisorption oxidation	
RMSD	Root-mean-square deviation	
RSSQ	Residual sum of squares	$mol^2\ L^{-2}$
QY	Quantum yield	$molecules\ photon^{-1}$

SAED	Selected area electron diffraction	
STY	Space time yield	molecules $\text{photon}^{-1}\ \text{mg}_{cat}^{-1}$
TBZ	Thiabendazole	
TEM	Transmission electron microscopy	
TPO	Temperature programmed oxidation	
T500	Zinc oxide reduced at 500°C	

Reference list

[1] P.C. Nagajyothi, S.V. Prabhakar Vattikuti, K.C. Devarayapalli, K. Yoo, J. Shim, T.V.M. Sreekanth, Green synthesis: Photocatalytic degradation of textile dyes using metal and metal oxide nanoparticles-latest trends and advancements, Crit. Rev. Environ. Sci. Technol., 50 (2020) 2617-2723.

[2] S. Deepracha, A. Ayral, M. Ogawa, Acceleration of the photocatalytic degradation of organics by in-situ removal of the products of degradation, Appl. Catal., B, 284 (2021) 119705.

[3] A. Ranjbari, N. Mokhtarani, Post treatment of composting leachate using ZnO nanoparticles immobilized on moving media, Appl. Catal., B, 220 (2018) 211-221.

[4] J. Li, Y. Xu, Z. Ding, A.H. Mahadi, Y. Zhao, Y.-F. Song, Photocatalytic selective oxidation of benzene to phenol in water over layered double hydroxide: A thermodynamic and kinetic perspective, Chem. Eng. J., 388 (2020) 124248.

[5] X. Pang, N. Skillen, N. Gunaratne, D.W. Rooney, P.K.J. Robertson, Removal of phthalates from aqueous solution by semiconductor photocatalysis: A review, J. Hazard. Mater., 402 (2021) 123461.

[6] B. Abebe, H.C.A. Murthy, E. Amare, Enhancing the photocatalytic efficiency of ZnO: Defects, heterojunction, and optimization, Environ. Nanotechnol. Monit. Manage., 14 (2020) 100336.

[7] Y. Fu, Z. Ren, J. Wu, Y. Li, W. Liu, P. Li, L. Xing, J. Ma, H. Wang, X. Xue, Direct Z-scheme heterojunction of ZnO/MoS_2 nanoarrays realized by flowing-induced piezoelectric field for enhanced sunlight photocatalytic performances, Appl. Catal., B, 285 (2021) 119785.

[8] M. Moradi, F. Hasanvandian, A.A. Isari, F. Hayati, B. Kakavandi, S.R. Setayesh, CuO and ZnO co-anchored on g-C_3N_4 nanosheets as an affordable double Z-scheme nanocomposite for photocatalytic decontamination of amoxicillin, Appl. Catal., B, 285 (2021) 119838.

[9] D.K. Sharma, S. Shukla, K.K. Sharma, V. Kumar, A review on ZnO: Fundamental properties and applications, Mater. Today:. Proc., (2020).

[10] M.M. Khan, N.H. Saadah, M.E. Khan, M.H. Harunsani, A.L. Tan, M.H. Cho, Potentials of Costus woodsonii leaf extract in producing narrow band gap ZnO nanoparticles, Mater. Sci. Semicond. Process., 91 (2019) 194-200.

[11] A.A. El-Bindary, S.M. El-Marsafy, A.A. El-Maddah, Enhancement of the photocatalytic activity of ZnO nanoparticles by silver doping for the degradation of AY99 contaminants, J. Mol. Struct., 1191 (2019) 76-84.

[12] A.E. Ramírez, M. Montero-Muñoz, L.L. López, J.E. Ramos-Ibarra, J.A.H. Coaquira, B. Heinrichs, C.A. Páez, Significantly enhancement of sunlight photocatalytic performance of ZnO by doping with transition metal oxides, Sci. Rep., 11 (2021) 2804.

[13] M. Lelis, S. Tuckute, S. Varnagiris, M. Urbonavicius, K. Bockute, G. Laukaitis, Synthesis and analysis of metallic Zn phase rich ZnO oxide films for the photocatalytic water treatment technologies, Mater. Today:. Proc., 33 (2020) 2484-2489.

[14] Q. Su, Y. Li, R. Hu, F. Song, S. Liu, C. Guo, S. Zhu, W. Liu, J. Pan, Heterojunction photocatalysts based on 2D materials: The role of configuration, Adv. Sustainable Syst., 4 (2020) 2000130.
[15] J. Li, X. Xu, X. Liu, C. Yu, D. Yan, Z. Sun, L. Pan, Sn doped TiO_2 nanotube with oxygen vacancy for highly efficient visible light photocatalysis, J. Alloys Compd., 679 (2016) 454-462.
[16] J.B. Park, Y.T. Chun, Y.B. Lee, J.I. Sohn, W.-K. Hong, Defect-mediated modulation of optical properties in vertically aligned ZnO nanowires via substrate-assisted Ga incorporation, J. Nanotechnol., 26 (2015) 145202.
[17] Y. Yu, B. Yao, Y. He, B. Cao, W. Ma, L. Chang, Oxygen defect-rich In-doped ZnO nanostructure for enhanced visible light photocatalytic activity, Mater. Chem. Phys., 244 (2020) 122672.
[18] Z. Zhang, W. Wang, E. Gao, M. Shang, J.J.J.o.h.m. Xu, Enhanced photocatalytic activity of Bi_2WO_6 with oxygen vacancies by zirconium doping, J. Hazard. Mater., 196 (2011) 255-262.
[19] P. Nandi, D. Das, Photocatalytic degradation of Rhodamine-B dye by stable ZnO nanostructures with different calcination temperature induced defects, Appl. Surf. Sci., 465 (2019) 546-556.
[20] Y. Lv, C. Pan, X. Ma, R. Zong, X. Bai, Y. Zhu, Production of visible activity and UV performance enhancement of ZnO photocatalyst via vacuum deoxidation, Appl. Catal., B, 138-139 (2013) 26-32.
[21] A.M. Mostafa, The enhancement of nonlinear absorption of Zn/ZnO thin film by creation oxygen vacancies via infrared laser irradiation and coating with Ag thin film via pulsed laser deposition, J. Mol. Struct., 1226 (2021) 129407.
[22] Z. Li, X. Liu, M. Zhou, S. Zhang, S. Cao, G. Lei, C. Lou, J. Zhang, Plasma-induced oxygen vacancies enabled ultrathin ZnO films for highly sensitive detection of triethylamine, J. Hazard. Mater., 415 (2021) 125757.
[23] Y. Lv, W. Yao, X. Ma, C. Pan, R. Zong, Y. Zhu, The surface oxygen vacancy induced visible activity and enhanced UV activity of a ZnO 1− x photocatalyst, Catal. Sci. Technol., 3 (2013) 3136-3146.
[24] P. Calza, S. Baudino, R. Aigotti, C. Baiocchi, E. Pelizzetti, Ion trap tandem mass spectrometric identification of thiabendazole phototransformation products on titanium dioxide, J. Chromatogr. A, 984 (2003) 59-66.
[25] R. Igual-Adell, C. Oltra-Alcaraz, E. Soler-Company, P. Sánchez-Sánchez, J. Matogo-Oyana, D. Rodríguez-Calabuig, Efficacy and safety of ivermectin and thiabendazole in the treatment of strongyloidiasis, Expert Opin. Pharmacother., 5 (2004) 2615-2619.
[26] A. Bernabeu, R. Vercher, L. Santos-Juanes, P. Simón, C. Lardín, M. Martínez, J. Vicente, R. González, C. Llosá, A. Arques, Solar photocatalysis as a tertiary treatment to remove emerging pollutants from wastewater treatment plant effluents, Catal. Today, 161 (2011) 235-240.
[27] C. Sirtori, A. Agüera, I. Carra, J.A.S. Pérez, Identification and monitoring of thiabendazole transformation products in water during Fenton degradation by LC-QTOF-MS, Anal. Bioanal.Chem., 406 (2014) 5323-5337.

[28] M. Jiménez, M. Ignacio Maldonado, E.M. Rodríguez, A. Hernández-Ramírez, E. Saggioro, I. Carra, J.A. Sanchez Perez, Supported TiO_2 solar photocatalysis at semi-pilot scale: degradation of pesticides found in citrus processing industry wastewater, reactivity and influence of photogenerated species, J. Chem. Technol. Biotechnol., 90 (2015) 149-157.

[29] S. Kumar, A. Kumar, A. Kumar, R. Balaji, V. Krishnan, Highly efficient visible light active 2D-2D nanocomposites of N-ZnO-g-C_3N_4 for photocatalytic degradation of diverse industrial pollutants, ChemistrySelect, 3 (2018) 1919-1932.

[30] A. Ranjbari, K. Demeestere, F. Verpoort, K.-H. Kim, P.M. Heynderickx, Novel kinetic modeling of thiabendazole removal by adsorption and photocatalysis on porous organic polymers: Effect of pH and visible light intensity, Chem. Eng. J., (2021) 133349.

[31] J.C. Garcia, K. Takashima, Photocatalytic degradation of imazaquin in an aqueous suspension of titanium dioxide, J. Photochem. Photobiol., A, 155 (2003) 215-222.

[32] J. Carbajo, A. Tolosana-Moranchel, J.A. Casas, M. Faraldos, A. Bahamonde, Analysis of photoefficiency in TiO_2 aqueous suspensions: Effect of titania hydrodynamic particle size and catalyst loading on their optical properties, Appl. Catal., B, 221 (2018) 1-8.

[33] X. Van Doorslaer, P.M. Heynderickx, K. Demeestere, K. Debevere, H. Van Langenhove, J. Dewulf, TiO_2 mediated heterogeneous photocatalytic degradation of moxifloxacin: operational variables and scavenger study, Appl. Catal., B, 111 (2012) 150-156.

[34] P. Makuła, M. Pacia, W. Macyk, How to correctly determine the band gap energy of modified semiconductor photocatalysts based on UV–Vis spectra, ACS Publications, J. Phys. Chem. Lett., 2018, pp. 6814-6817.

[35] Q. Zhang, M. Xu, B. You, Q. Zhang, H. Yuan, K. Ostrikov, Oxygen vacancy-mediated ZnO nanoparticle photocatalyst for degradation of methylene blue, Appl. Sci., 8 (2018) 353.

[36] C.K. Cheng, S.Y. Foo, A.A. Adesina, Glycerol steam reforming over bimetallic Co−Ni/Al_2O_3, Ind. Eng. Chem. Res., 49 (2010) 10804-10817.

[37] A. Gervasini, Temperature Programmed Reduction/Oxidation (TPR/TPO) Methods, Calorimetry and Thermal Methods in Catalysis, Springer2013, pp. 175-195.

[38] E. Cerrato, M.C. Paganini, E. Giamello, Photoactivity under visible light of defective ZnO investigated by EPR spectroscopy and photoluminescence, J. Photochem. Photobiol., A, 397 (2020) 112531.

[39] H. Kaftelen, K. Ocakoglu, R. Thomann, S. Tu, S. Weber, E. Erdem, EPR and photoluminescence spectroscopy studies on the defect structure of ZnO nanocrystals, Phys. Rev. B, 86 (2012) 014113.

[40] A.J. Reddy, M. Kokila, H. Nagabhushana, R. Chakradhar, C. Shivakumara, J. Rao, B. Nagabhushana, Structural, optical and EPR studies on ZnO: Cu nanopowders prepared via low temperature solution combustion synthesis, J. Alloys Compd., 509 (2011) 5349-5355.

[41] S. Polarz, J. Strunk, V. Ischenko, M.W. Van den Berg, O. Hinrichsen, M. Muhler, M. Driess, On the role of oxygen defects in the catalytic performance of zinc oxide, Angew. Chem. Int. Ed., 45 (2006) 2965-2969.

[42] C. Drouilly, J.-M. Krafft, F. Averseng, S. Casale, D. Bazer-Bachi, C. Chizallet, V. Lecocq, H. Vezin, H.l.n. Lauron-Pernot, G. Costentin, ZnO oxygen vacancies formation and filling followed by in situ photoluminescence and in situ EPR, J. Phys. Chem. C, 116 (2012) 21297-21307.
[43] S. Locmelis, C. Brünig, M. Binnewies, A. Börger, K.D. Becker, T. Homann, T. Bredow, Optical band gap in the system $ZnO_{1-x}S_x$. An experimental and quantum chemical study, J. Mater. Sci., 42 (2007) 1965-1971.
[44] X. Liang, P. Wang, Y. Gao, H. Huang, F. Tong, Q. Zhang, Z. Wang, Y. Liu, Z. Zheng, Y. Dai, B. Huang, Design and synthesis of porous M-ZnO/CeO_2 microspheres as efficient plasmonic photocatalysts for nonpolar gaseous molecules oxidation: Insight into the role of oxygen vacancy defects and M=Ag, Au nanoparticles, Appl. Catal., B, 260 (2020) 118151.
[45] I. Hegazy, R. Geioushy, S. El-Sheikh, A. Shawky, S. El-Sherbiny, A.-H.T. Kandil, Influence of oxygen vacancies on the performance of ZnO nanoparticles towards CO_2 photoreduction in different aqueous solutions, J. Environ. Chem. Eng., 8 (2020) 103887.
[46] F.-M. Chang, S. Brahma, J.-H. Huang, Z.-Z. Wu, K.-Y. Lo, Strong correlation between optical properties and mechanism in deficiency of normalized self-assembly ZnO nanorods, Sci. Rep., 9 (2019) 1-9.
[47] M. Ji, R. Chen, J. Di, Y. Liu, K. Li, Z. Chen, J. Xia, H. Li, Oxygen vacancies modulated Bi-rich bismuth oxyiodide microspheres with tunable valence band position to boost the photocatalytic activity, J. Colloid Interface Sci., 533 (2019) 612-620.
[48] X. Wang, Y. Zhang, C. Zhou, D. Huo, R. Zhang, L. Wang, Hydroxyl-regulated BiOI nanosheets with a highly positive valence band maximum for improved visible-light photocatalytic performance, Appl. Catal., B, 268 (2020) 118390.
[49] C. Feng, F. Teng, Z. Liu, C. Chang, Y. Zhao, S. Wang, M. Chen, W. Yao, Y. Zhu, A newly discovered BiF_3 photocatalyst with a high positive valence band, J. Mol. Catal. A: Chem., 401 (2015) 35-40.
[50] N. Kamarulzaman, M.F. Kasim, R. Rusdi, Band gap narrowing and widening of ZnO nanostructures and doped materials, Nanoscale Res. Lett., 10 (2015) 1-12.
[51] P. Jubu, F. Yam, V. Igba, K. Beh, Tauc-plot scale and extrapolation effect on bandgap estimation from UV–vis–NIR data–a case study of β-Ga_2O_3, J. Solid State Chem., 290 (2020) 121576.
[52] H.-L. Guo, Q. Zhu, X.-L. Wu, Y.-F. Jiang, X. Xie, A.-W. Xu, Oxygen deficient ZnO_{1-x} nanosheets with high visible light photocatalytic activity, Nanoscale, 7 (2015) 7216-7223.
[53] D.-P. Bui, M.-T. Pham, H.-H. Tran, T.-D. Nguyen, T.M. Cao, V.V. Pham, Revisiting the key optical and electrical characteristics in reporting the photocatalysis of semiconductors, ACS Omega, 6 (2021) 27379-27386.
[54] S. Huang, J. Zhong, J. Li, J. Chen, Z. Xiang, W. Hu, M. Li, Z-scheme TiO_2/g-C_3N_4 composites with improved solar-driven photocatalytic performance deriving from remarkably efficient separation of photo-generated charge pairs, Mater. Res. Bull., 84 (2016) 65-70.

[55] D. Ma, J. Zhong, J. Li, C. Burda, R. Duan, Preparation and photocatalytic performance of MWCNTs/BiOCl: Evidence for the superoxide radical participation in the degradation mechanism of phenol, Appl. Surf. Sci., 480 (2019) 395-403.

[56] N. Tu, K. Nguyen, D. Trung, N. Tuan, V.N. Do, P. Huy, Effects of carbon on optical properties of ZnO powder, J. Lumin., 174 (2016) 6-10.

[57] S. Muthukumaran, R. Gopalakrishnan, Structural, FTIR and photoluminescence studies of Cu doped ZnO nanopowders by co-precipitation method, Opt. Mater., 34 (2012) 1946-1953.

[58] N. Tu, H. Van Bui, D. Trung, A.-T. Duong, D. Thuy, D. Nguyen, K. Nguyen, P. Huy, Surface oxygen vacancies of ZnO: a facile fabrication method and their contribution to the photoluminescence, J. Alloys Compd., 791 (2019) 722-729.

[59] N. Alvi, O. Nur, M. Willander, The origin of the red emission in n-ZnO nanotubes/p-GaN white light emitting diodes, Nanoscale Res. Lett., 6 (2011) 1-7.

[60] V.D. Mote, Y. Purushotham, B.N. Dole, Williamson-Hall analysis in estimation of lattice strain in nanometer-sized ZnO particles, J. Theor. Appl. Phys., 6 (2012) 6.

[61] L.H. Kathwate, G. Umadevi, P.M. Kulal, P. Nagaraju, D.P. Dubal, A.K. Nanjundan, V.D. Mote, Ammonia gas sensing properties of Al doped ZnO thin films, Sens. Actuators, A, 313 (2020) 112193.

[62] P. Shankar, M.Q.H. Ishak, J.K. Padarti, N. Mintcheva, S. Iwamori, S.O. Gurbatov, J.H. Lee, S.A. Kulinich, ZnO graphene oxide core shell nanoparticles prepared via one-pot approach based on laser ablation in water, Appl. Surf. Sci., 531 (2020) 147365.

[63] A. Katiyar, N. Kumar, R.K. Shukla, A. Srivastava, Substrate free defect-rich one dimensional ZnO nanostructures, Mater. Today:. Proc., 46 (2021) 2374-2378.

[64] O. Bazta, A. Urbieta, S. Trasobares, J. Piqueras, P. Fernández, M. Addou, J.J. Calvino, A.B. Hungría, In-depth structural and optical analysis of Ce-modified ZnO nanopowders with enhanced photocatalytic activity prepared by microwave-assisted hydrothermal method, Catalysts, 10 (2020) 551.

[65] K. Karmakar, A. Sarkar, K. Mandal, G.G. Khan, Investigating the role of oxygen vacancies and lattice strain defects on the enhanced photoelectrochemical property of alkali metal (Li, Na, and K) doped ZnO nanorod photoanodes, ChemElectroChem, 5 (2018) 1147-1152.

[66] H. Chang, E. Bjørgum, O. Mihai, J. Yang, H.L. Lein, T. Grande, S. Raaen, Y.-A. Zhu, A. Holmen, D. Chen, Effects of oxygen mobility in La–Fe-based perovskites on the catalytic activity and selectivity of methane oxidation, ACS Catal., 10 (2020) 3707-3719.

[67] S. Mustapha, M.M. Ndamitso, A.S. Abdulkareem, J.O. Tijani, D.T. Shuaib, A.K. Mohammed, A. Sumaila, Comparative study of crystallite size using Williamson-Hall and Debye-Scherrer plots for ZnO nanoparticles, Adv. Nat. Sci.: Nanosci. Nanotechnol., 10 (2019) 045013.

[68] M. Kubicek, Z. Cai, W. Ma, B. Yildiz, H. Hutter, J. Fleig, Tensile lattice strain accelerates oxygen surface exchange and diffusion in $La_{1-x}Sr_xCoO_{3-\delta}$ thin films, ACS Nano, 7 (2013) 3276-3286.

[69] Y. Pang, Y. Liu, X. Zhang, M. Gao, H. Pan, Role of particle size, grain size, microstrain and lattice distortion in improved dehydrogenation properties of the ball-milled $Mg(AlH_4)_2$, Int. J. Hydrogen Energy, 38 (2013) 1460-1468.

[70] J.A. Moulijn, A.E. van Diepen, F. Kapteijn, Catalyst deactivation: is it predictable?: What to do?, Appl. Catal., A, 212 (2001) 3-16.

[71] M.B. Fichtl, D. Schlereth, N. Jacobsen, I. Kasatkin, J. Schumann, M. Behrens, R. Schlögl, O. Hinrichsen, Kinetics of deactivation on $Cu/ZnO/Al_2O_3$ methanol synthesis catalysts, Appl. Catal., A, 502 (2015) 262-270.

[72] W. Wang, P. Liu, M. Zhang, J. Hu, F. Xing, The Pore Structure of Phosphoaluminate Cement, J. Compos. Mater., Vol.02No.03 (2012) 9.

[73] L. Yang, L. Pastor-Pérez, S. Gu, A. Sepúlveda-Escribano, T.R. Reina, Highly efficient Ni/CeO_2-Al_2O_3 catalysts for CO_2 upgrading via reverse water-gas shift: Effect of selected transition metal promoters, Appl. Catal., B, 232 (2018) 464-471.

[74] H. Qian, G. Yu, Q. Hou, Y. Nie, C. Bai, X. Bai, H. Wang, M. Ju, Ingenious control of adsorbed oxygen species to construct dual reaction centers ZnO@FePc photo-Fenton catalyst with high-speed electron transmission channel for PPCPs degradation, Appl. Catal., B, 291 (2021) 120064.

[75] H. Ennajih, H. Gueddar, A. El Kadib, R. Bouhfid, M. Bousmina, E.M. Essassi, Intercalation of nickel and cobalt thiabendazole complexes into montmorillonite, Appl. Clay Sci., 65 (2012) 139-142.

[76] M.J. Oliveira, R.J. Rubira, L.N. Furini, A. Batagin-Neto, C.J. Constantino, Detection of thiabendazole fungicide/parasiticide by SERS: quantitative analysis and adsorption mechanism, Appl. Surf. Sci., 517 (2020) 145786.

[77] K. Aziz, F. Aziz, R. Mamouni, L. Aziz, Z. Anfar, A. Azrrar, B. Kjidaa, N. Saffaj, A. Laknifli, High thiabendazole fungicide uptake using *Cellana tramoserica* shells modified by copper: characterization, adsorption mechanism, and optimization using CCD-RSM approach, Environ. Sci. Pollut. Res., (2021) 1-16.

[78] A. Ahmed, Y. Chaker, E.H. Belarbi, O. Abbas, J. Chotard, H. Abassi, A.N. Van Nhien, M. El Hadri, S. Bresson, XRD and ATR/FTIR investigations of various montmorillonite clays modified by monocationic and dicationic imidazolium ionic liquids, J. Mol. Struct., 1173 (2018) 653-664.

[79] Q. Lv, N. Wang, W. Si, Z. Hou, X. Li, X. Wang, F. Zhao, Z. Yang, Y. Zhang, C. Huang, Pyridinic nitrogen exclusively doped carbon materials as efficient oxygen reduction electrocatalysts for Zn-air batteries, Appl. Catal., B, 261 (2020) 118234.

[80] S. Liu, J. Zhou, H. Song, Tailoring Highly N-Doped Carbon Materials from Hexamine-Based MOFs: Superior Performance and New Insight into the Roles of N Configurations in Na-Ion Storage, Small, 14 (2018) 1703548.

[81] K. Yu, L.-L. Lou, S. Liu, W. Zhou, Asymmetric oxygen vacancies: the intrinsic redox active sites in metal oxide catalysts, Adv. Sci., 7 (2020) 1901970.

[82] J. Hu, X. Zhao, W. Chen, Z. Chen, Enhanced charge transport and increased active sites on α-Fe_2O_3 (110) nanorod surface containing oxygen vacancies for improved solar water oxidation performance, ACS Omega, 3 (2018) 14973-14980.

[83] B. Lombardi, M. Baschini, R.M. Torres Sánchez, Optimization of parameters and adsorption mechanism of thiabendazole fungicide by a montmorillonite of North Patagonia, Argentina, Appl. Clay Sci., 24 (2003) 43-50.
[84] K.S. Suganthi, K.S. Rajan, Temperature induced changes in ZnO–water nanofluid: Zeta potential, size distribution and viscosity profiles, Int. J. Heat Mass Transfer, 55 (2012) 7969-7980.
[85] D. Pinheiro, K.S. Devi, A. Jose, N.R. Bharadwaj, K. Thomas, Effect of surface charge and other critical parameters on the adsorption of dyes on SLS coated ZnO nanoparticles and optimization using response surface methodology, J. Environ. Chem. Eng., 8 (2020) 103987.
[86] W.Z. Tang, C.P. Huang, Photocatalyzed oxidation pathways of 2,4-dichlorophenol by CdS in basic and acidic aqueous solutions, Water Res., 29 (1995) 745-756.
[87] S. Tunesi, M. Anderson, Influence of chemisorption on the photodecomposition of salicylic acid and related compounds using suspended titania ceramic membranes, J. Phys. Chem., 95 (1991) 3399-3405.
[88] I.K. Konstantinou, T.A. Albanis, Photocatalytic transformation of pesticides in aqueous titanium dioxide suspensions using artificial and solar light: intermediates and degradation pathways, Appl. Catal., B, 42 (2003) 319-335.
[89] D. Ma, L. Yang, Z. Sheng, Y. Chen, Photocatalytic degradation mechanism of benzene over $ZnWO_4$: Revealing the synergistic effects of Na-doping and oxygen vacancies, Chem. Eng. J., 405 (2021) 126538.
[90] P. Wang, X. Li, S. Fan, X. Chen, M. Qin, D. Long, M.O. Tadé, S. Liu, Impact of oxygen vacancy occupancy on piezo-catalytic activity of $BaTiO_3$ nanobelt, Appl. Catal., B, 279 (2020) 119340.
[91] N. Zhang, C. Gao, Y. Xiong, Defect engineering: A versatile tool for tuning the activation of key molecules in photocatalytic reactions, J. Energy Chem., 37 (2019) 43-57.
[92] L. Wang, Y. Cai, B. Liu, L. Dong, A facile synthesis of brown anatase TiO_2 rich in oxygen vacancies and its visible light photocatalytic property, Solid State Ionics, 361 (2021) 115564.
[93] L. Hou, M. Zhang, Z. Guan, Q. Li, J. Yang, Effect of annealing ambience on the formation of surface/bulk oxygen vacancies in TiO_2 for photocatalytic hydrogen evolution, Appl. Surf. Sci., 428 (2018) 640-647.
[94] J. Smitka, A. Lemos, M. Porel, S. Jockusch, T.R. Belderrain, E. Tesařová, J.P. Da Silva, Phototransformation of benzimidazole and thiabendazole inside cucurbit [8] uril, Photochem. Photobiol. Sci., 13 (2014) 310-315.
[95] I. Carra, C. Sirtori, L. Ponce-Robles, J.A. Sánchez Pérez, S. Malato, A. Agüera, Degradation and monitoring of acetamiprid, thiabendazole and their transformation products in an agro-food industry effluent during solar photo-Fenton treatment in a raceway pond reactor, Chemosphere, 130 (2015) 73-81.
[96] C. Sirtori, A. Agüera, I. Carra, J.A. Sanchéz Pérez, Identification and monitoring of thiabendazole transformation products in water during Fenton degradation by LC-QTOF-MS, Anal. Bioanal.Chem., 406 (2014) 5323-5337.

[97] N. Raza, W. Raza, H. Gul, M. Azam, J. Lee, K. Vikrant, K.-H. Kim, Solar-light-active silver phosphate/titanium dioxide/silica heterostructures for photocatalytic removal of organic dye, J. Cleaner Prod., 254 (2020) 120031.

[98] H. Yan, R. Wang, R. Liu, T. Xu, J. Sun, L. Liu, J. Wang, Recyclable and reusable direct Z-scheme heterojunction CeO_2/TiO_2 nanotube arrays for photocatalytic water disinfection, Appl. Catal., B, 291 (2021) 120096.

[99] J. Strunk, W.C. Vining, A.T. Bell, A study of oxygen vacancy formation and annihilation in submonolayer coverages of TiO_2 dispersed on MCM-48, J. Phys. Chem. C, 114 (2010) 16937-16945.

[100] S.Y. Ryu, N.Y. Ha, Y.H. Ahn, J.-Y. Park, S. Lee, Effects of Oxygen Vacancies in a Zinc Oxide Electron Transport Layer on Long-Term Degradation and Short-Term Photo-Induced Changes in the Operation Characteristics of Organic Solar Cells, ACS Appl. Energy Mater., 5 (2022) 9668-9675.

[101] J. Li, L. Liu, Q. Liang, M. Zhou, C. Yao, S. Xu, Z. Li, Core-shell ZIF-8@MIL-68(In) derived ZnO nanoparticles-embedded In_2O_3 hollow tubular with oxygen vacancy for photocatalytic degradation of antibiotic pollutant, J. Hazard. Mater., 414 (2021) 125395.

[102] Y. Liu, Q. Zhang, M. Xu, H. Yuan, Y. Chen, J. Zhang, K. Luo, J. Zhang, B. You, Novel and efficient synthesis of Ag-ZnO nanoparticles for the sunlight-induced photocatalytic degradation, Appl. Surf. Sci., 476 (2019) 632-640.

[103] Y. Xu, H. Li, B. Sun, P. Qiao, L. Ren, G. Tian, B. Jiang, K. Pan, W. Zhou, Surface oxygen vacancy defect-promoted electron-hole separation for porous defective ZnO hexagonal plates and enhanced solar-driven photocatalytic performance, Chem. Eng. J., 379 (2020) 122295.

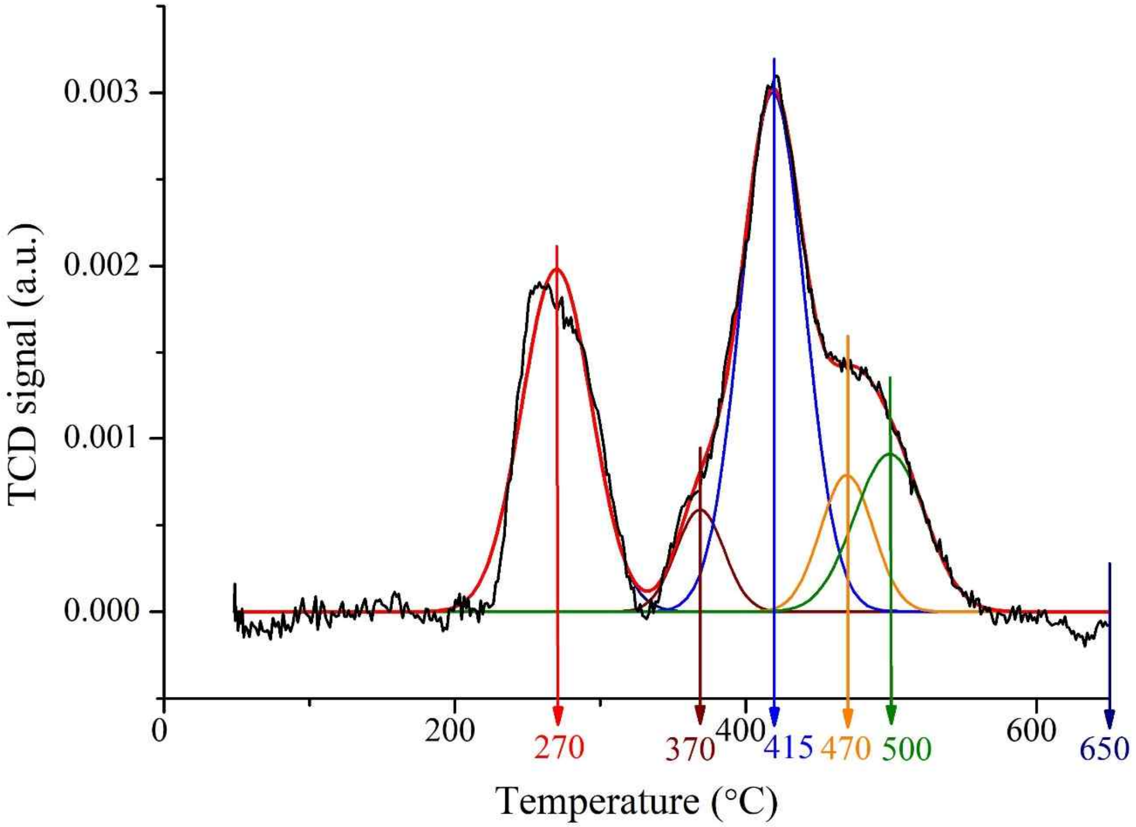

Figure 1. Results for H_2-TPR of commercial ZnO. Sample mass 200 mg, flow gas 10% H_2/Ar, flowrate 60 cm^3/min, temperature ramp 10 °C/min. Y-axis is the value of thermal conductivity detector (TCD) of the Autochem II equipment.

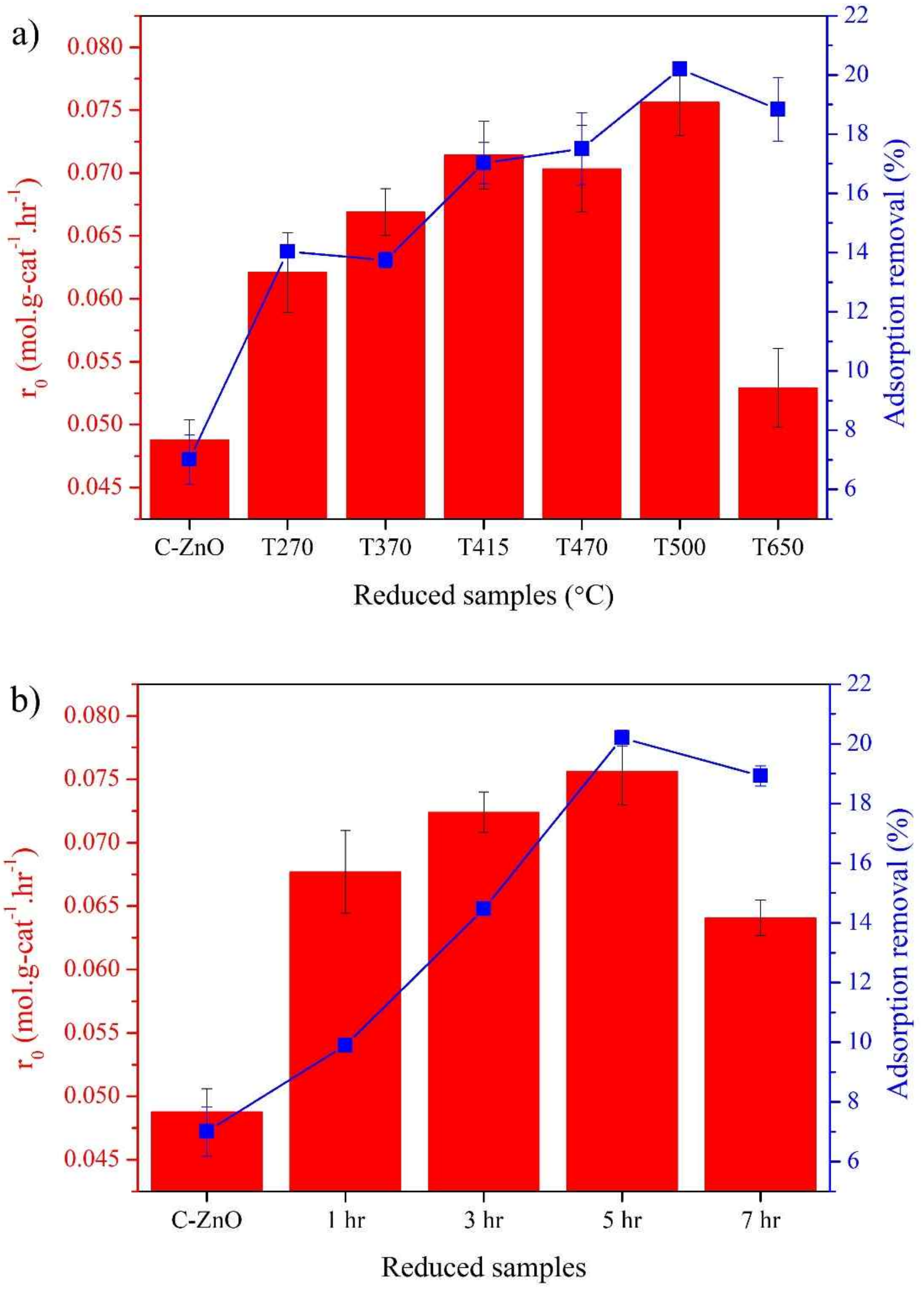

Figure 2. Optimization of the reduction temperature and time: a) effect of reduction temperature at 5 hours' reduction time, and b) effect of reduction time at a reduction temperature of 500°C on the initial reaction rate (bars) and adsorption removal (symbols) of thiabendazole. ZnO 500 mg/L, pH 7, initial thiabendazole concentration 10 mg/L.

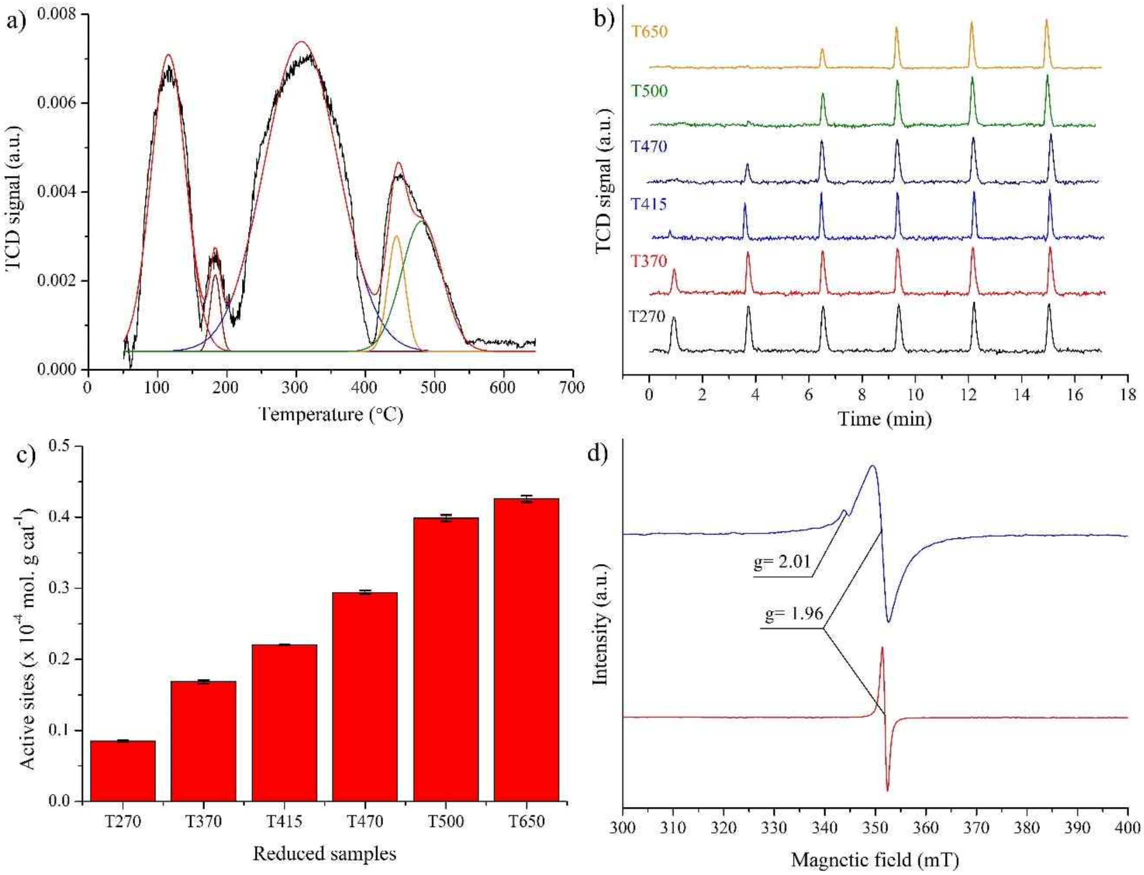

Figure 3. TPO and PCO results. a) TPO analysis of T500 catalyst, sample mass 200 mg, flow gas 5% O_2/Ar, flowrate 30 cm^3/min, temperature ramp 10 °C/min. b) PCO of reduced catalysts at different temperatures, sample mass 200 mg, carrier gas Ar with flowrate of 30 cm^3/min, loop gas 5% O_2/Ar with loop volume of 0.486 cm^3. c) Calculated amount of active sites created by hydrogen reduction at different temperatures using PCO data in graph b. d) EPR spectra of C-ZnO (—) and T500 (—) catalysts.

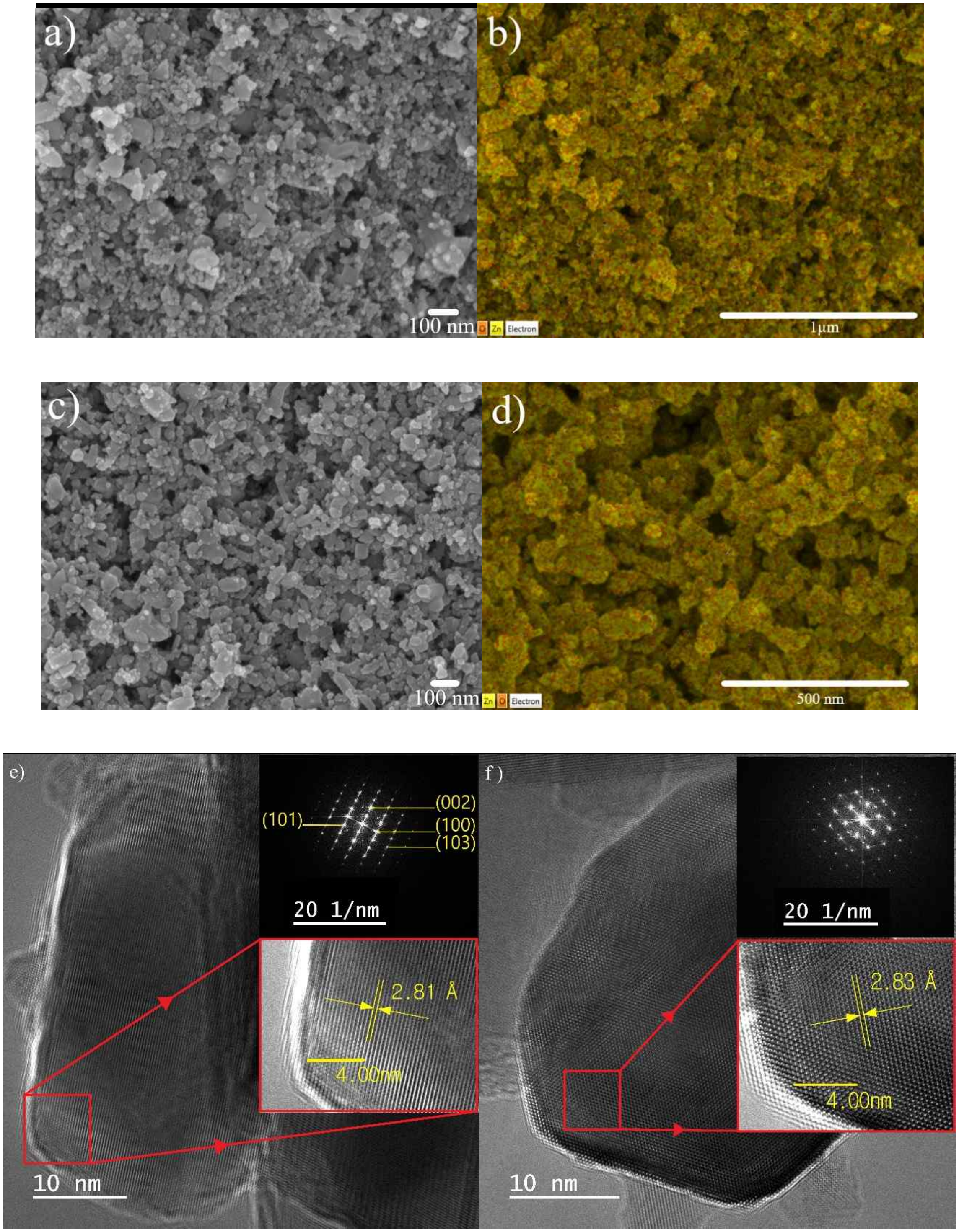

Figure 4. Results of FE-SEM, HR-TEM, and EDS analysis of ZnO: a) FE-SEM of C-ZnO, b) EDS of C-ZnO, c) FE-SEM of T500, d) EDS of T500, e) HR-TEM of C-ZnO, and f) HR-TEM of T500.

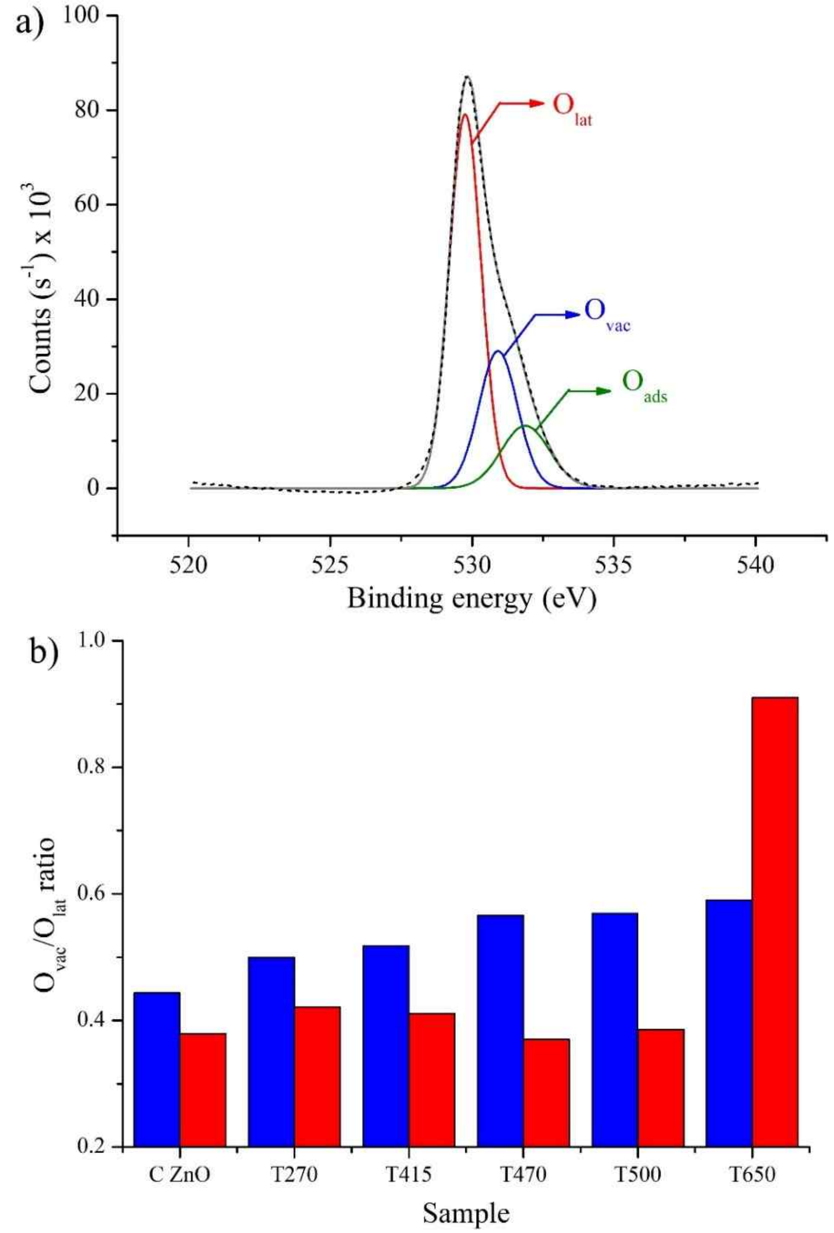

Figure 5. Surface and depth XPS of the O 1s spectrum of different ZnO catalysts: a) O1s spectrum at the surface of C-ZnO and b) O_{vac}/O_{lat} ratio at the surface and depth of different ZnO catalysts. (▬) lattice oxygen, (▬) vacancy oxygen, (▬) adsorbed oxygen, (▬) cumulative plot, (- - -) original spectrum, (🟦) O_{vac}/O_{lat} at the surface, (🟥) O_{vac}/O_{lat} at the depth.

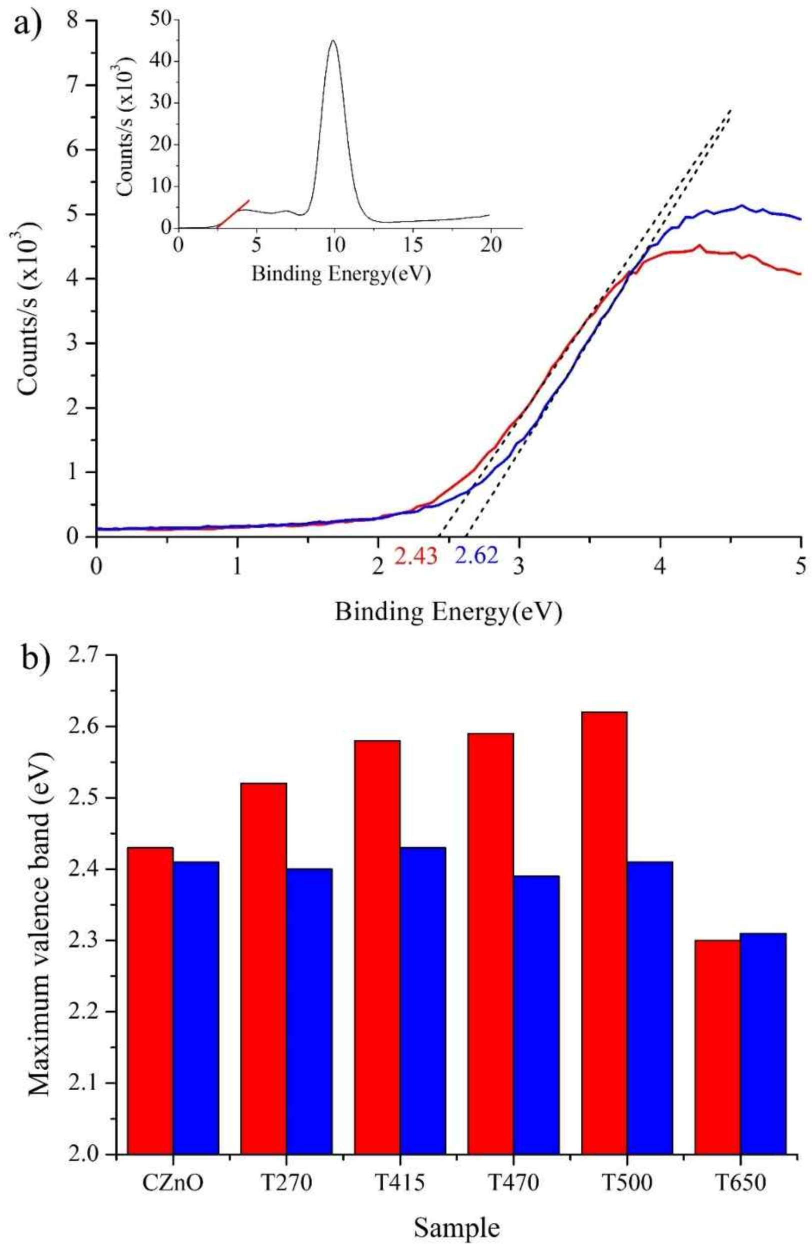

Figure 6. Maximum valence band as determined from the surface XPS spectrum: a) surface XPS spectrum for maximum valence band (C-ZnO (▬) and T500 (▬)), and b) comparison of maximum valence band of different ZnO catalysts (surface XPS spectrum (🟥) and deep XPS spectrum (🟦)).

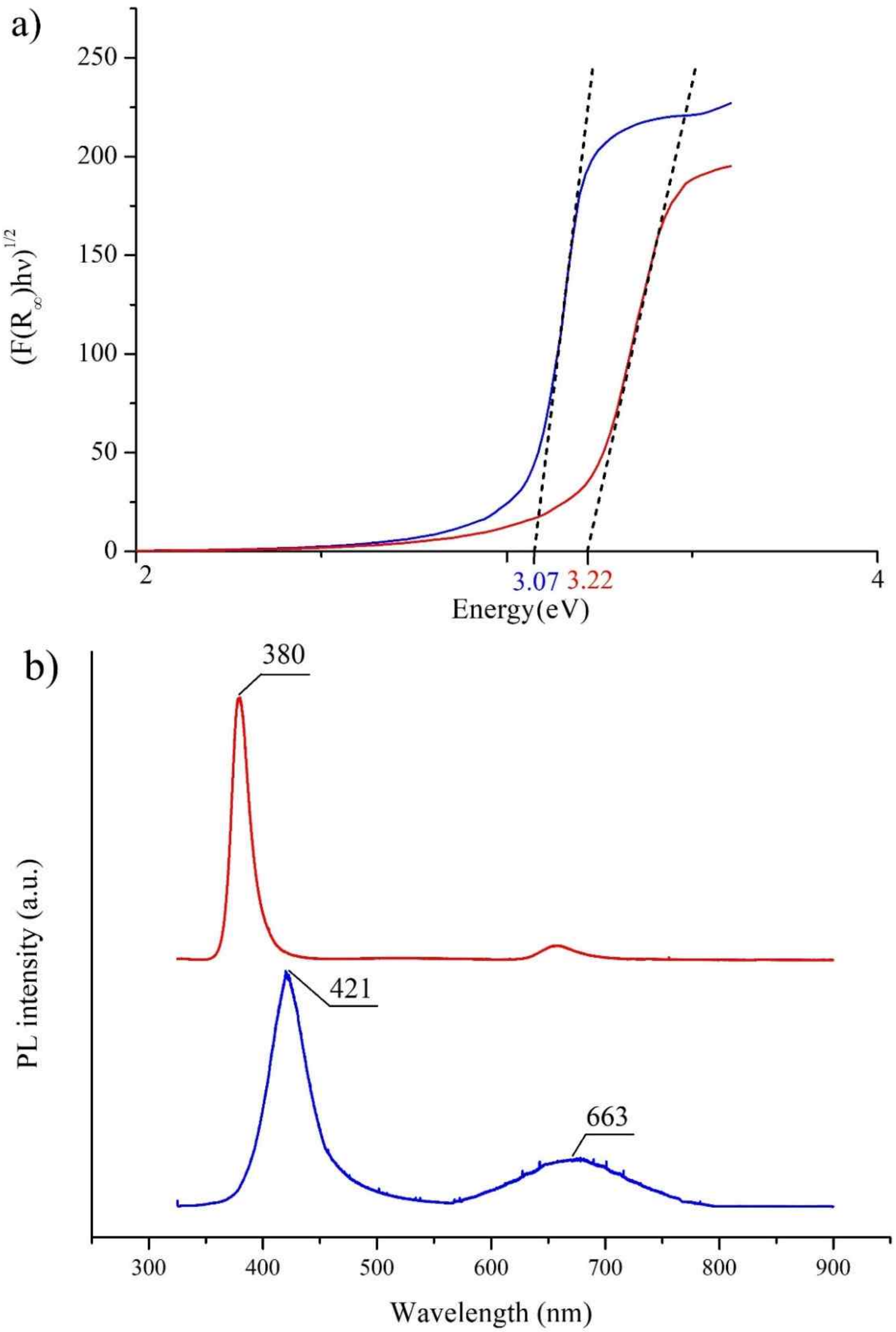

Figure 7. Optical properties of the catalysts: a) Tauc plot, and b) PL spectra of C-ZnO (🟥) and T500 (🟦) catalyst.

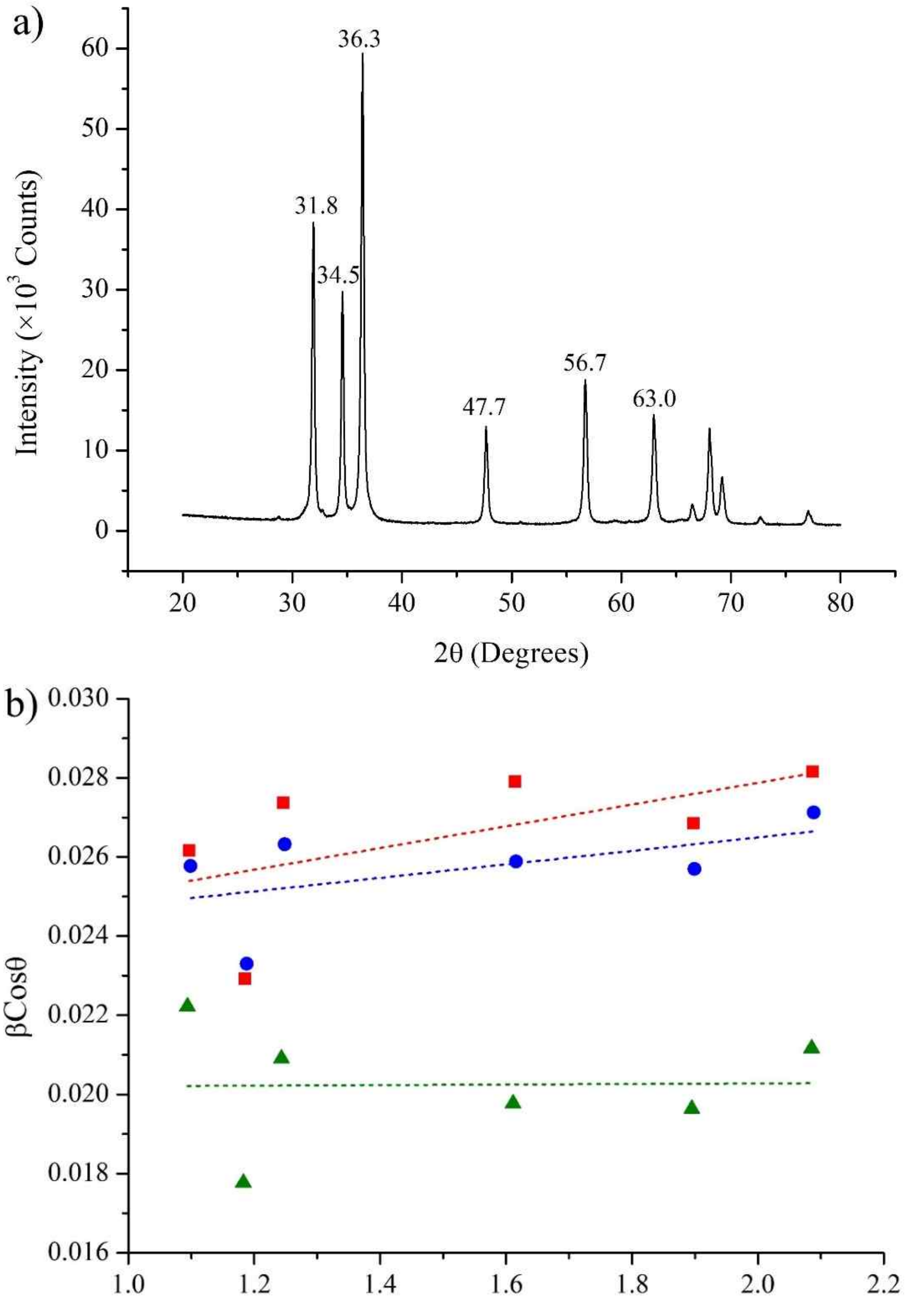

Figure 8. XRD characterization of different ZnO catalysts: a) XRD spectrum of T500. b) Williamson-Hall plot for C-ZnO (🟥), T500 (●), and T650 (▲).

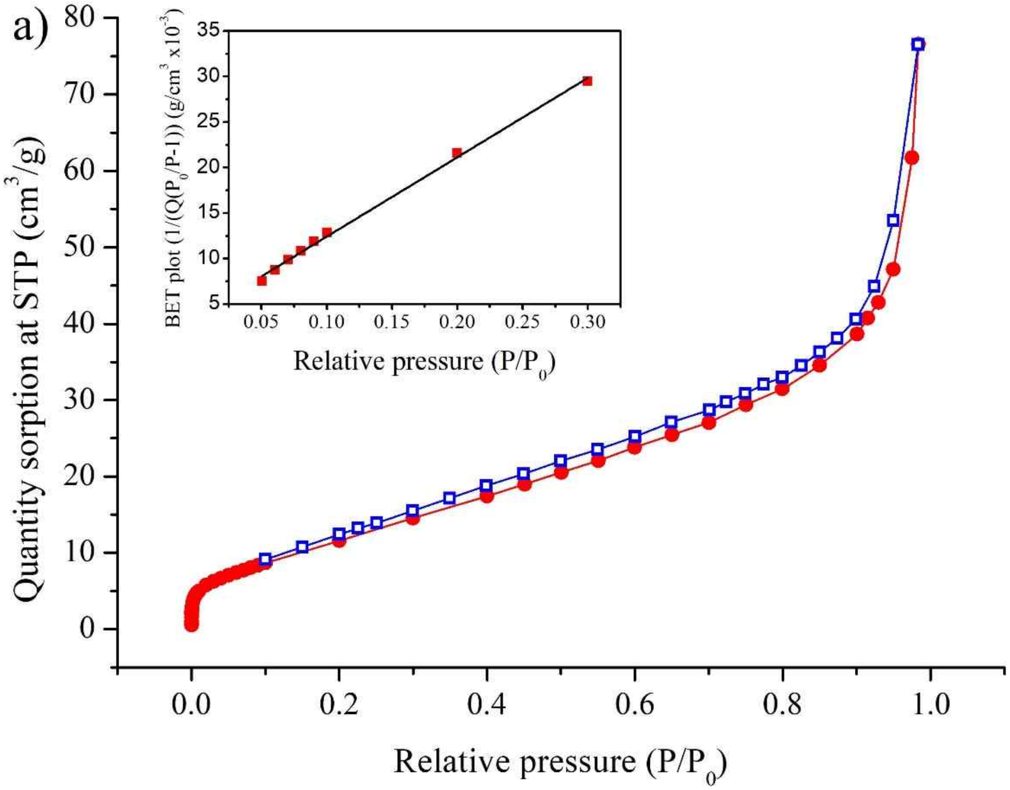
a)
Quantity sorption at STP (cm^3/g)
0
10
20
30
40
50
60
70
80
0.0
0.2
0.4
0.6
0.8
1.0
Relative pressure (P/P$_0$)
BET plot (1/(Q(P$_0$/P-1)) (g/cm^3 x10^{-3})
5
10
15
20
25
30
35
0.05
0.10
0.15
0.20
0.25
0.30
Relative pressure (P/P$_0$)

1194

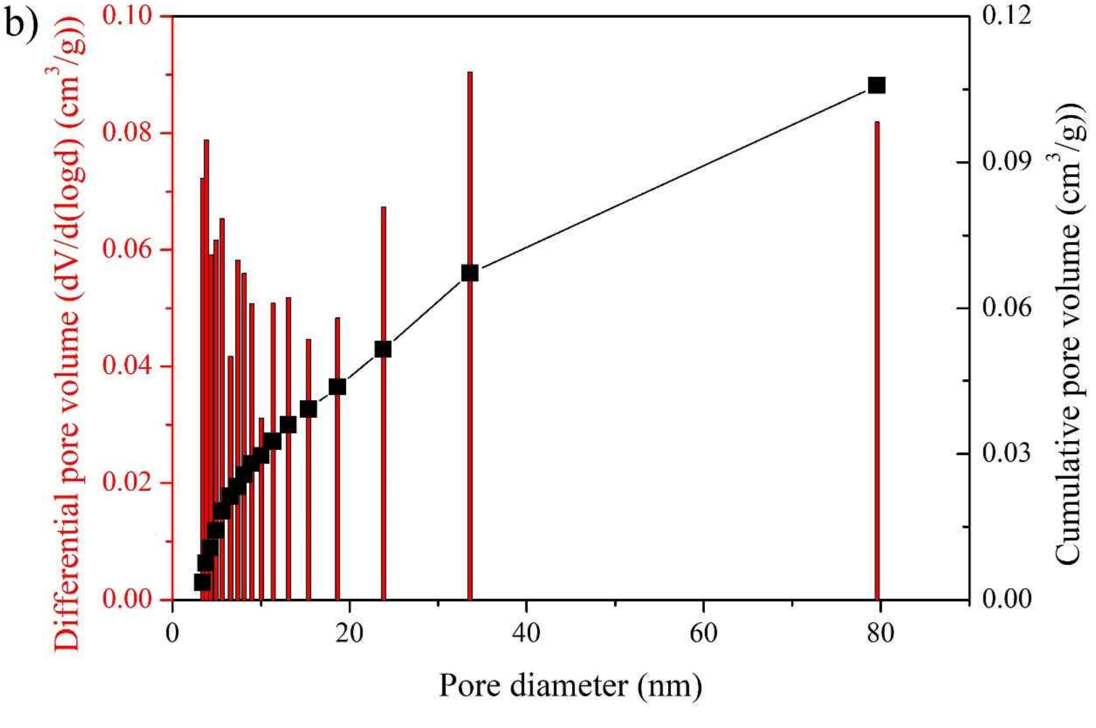
b)
Differential pore volume (dV/d(logd) (cm^3/g))
0.00
0.02
0.04
0.06
0.08
0.10
0
20
40
60
80
Pore diameter (nm)
Cumulative pore volume (cm^3/g))
0.00
0.03
0.06
0.09
0.12

1195

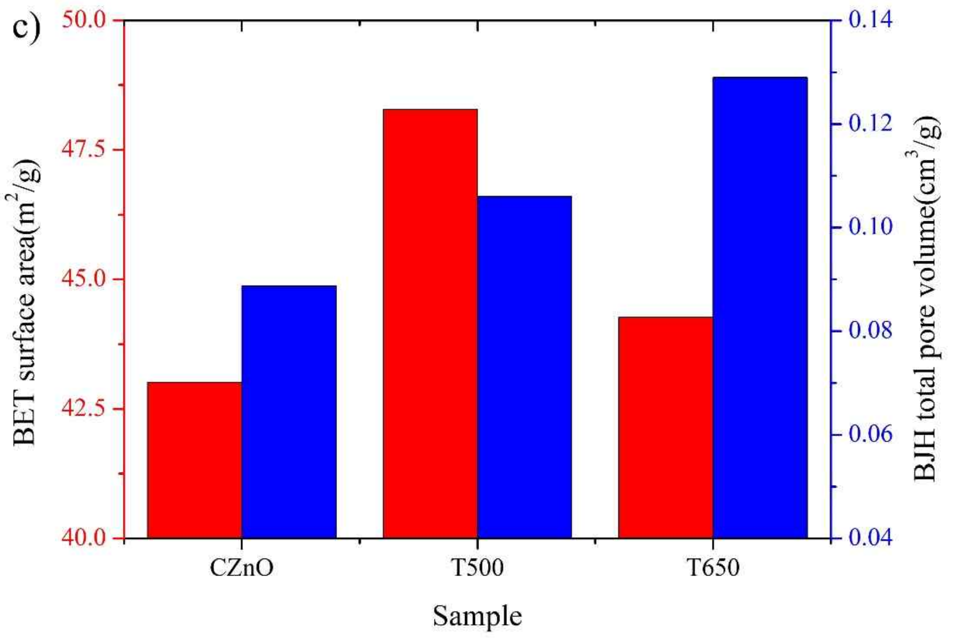

Figure 9. Surface area and pore characteristics of the catalysts: a) adsorption-desorption isotherms of T500, (●) adsorption, (□) desorption. b) BJH pore distribution of T500, (■) differential pore volume, (■) cumulative pore volume. c) comparison of (■) BET surface area and (■) BJH total pore volume of the catalysts.

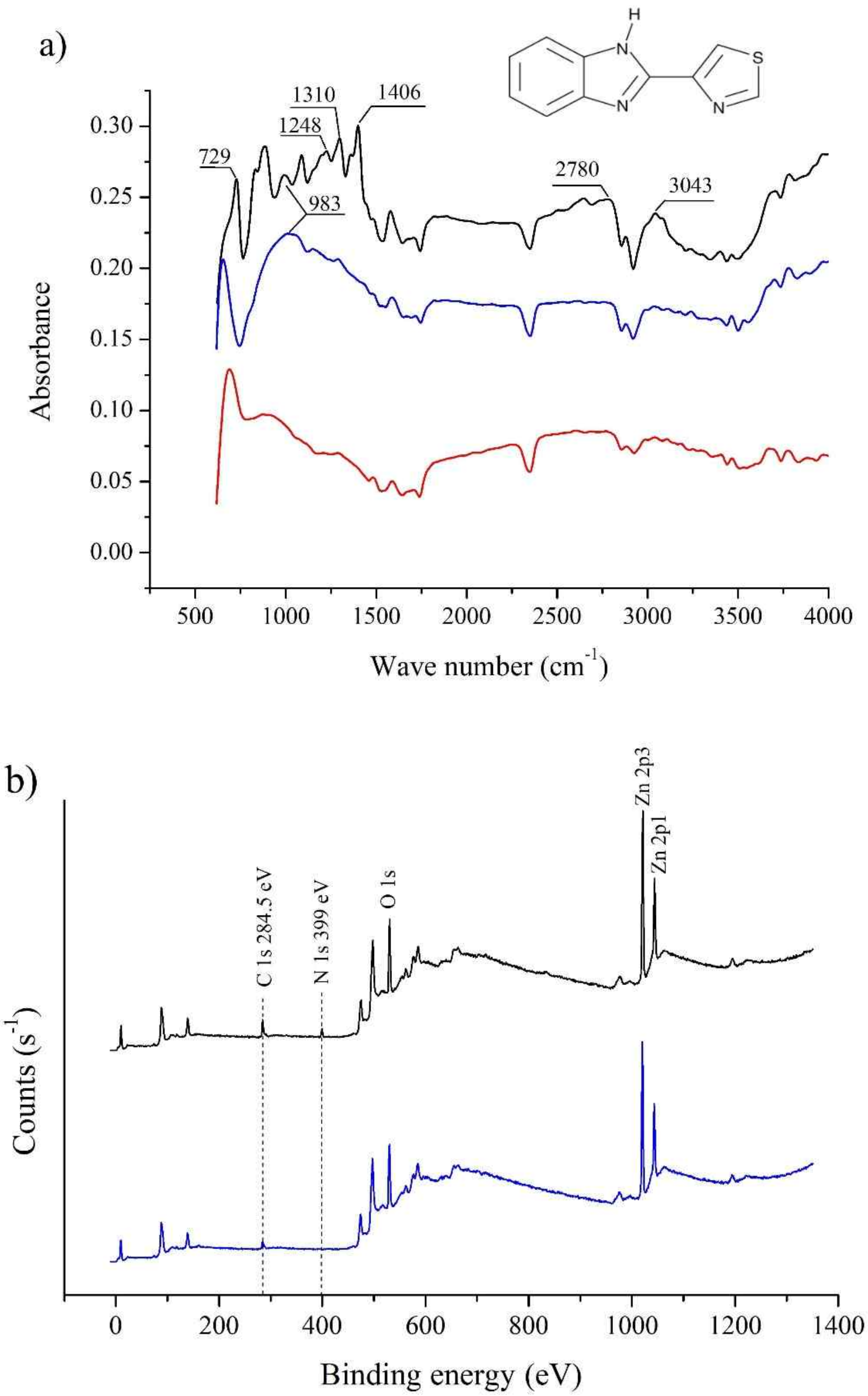

Figure 10. a) FTIR spectra of C-ZnO (—), and T500 (—), and T500 after adsorption of TBZ (—). b) XPS spectra of T500 (—), and T500 after adsorption of TBZ (—).

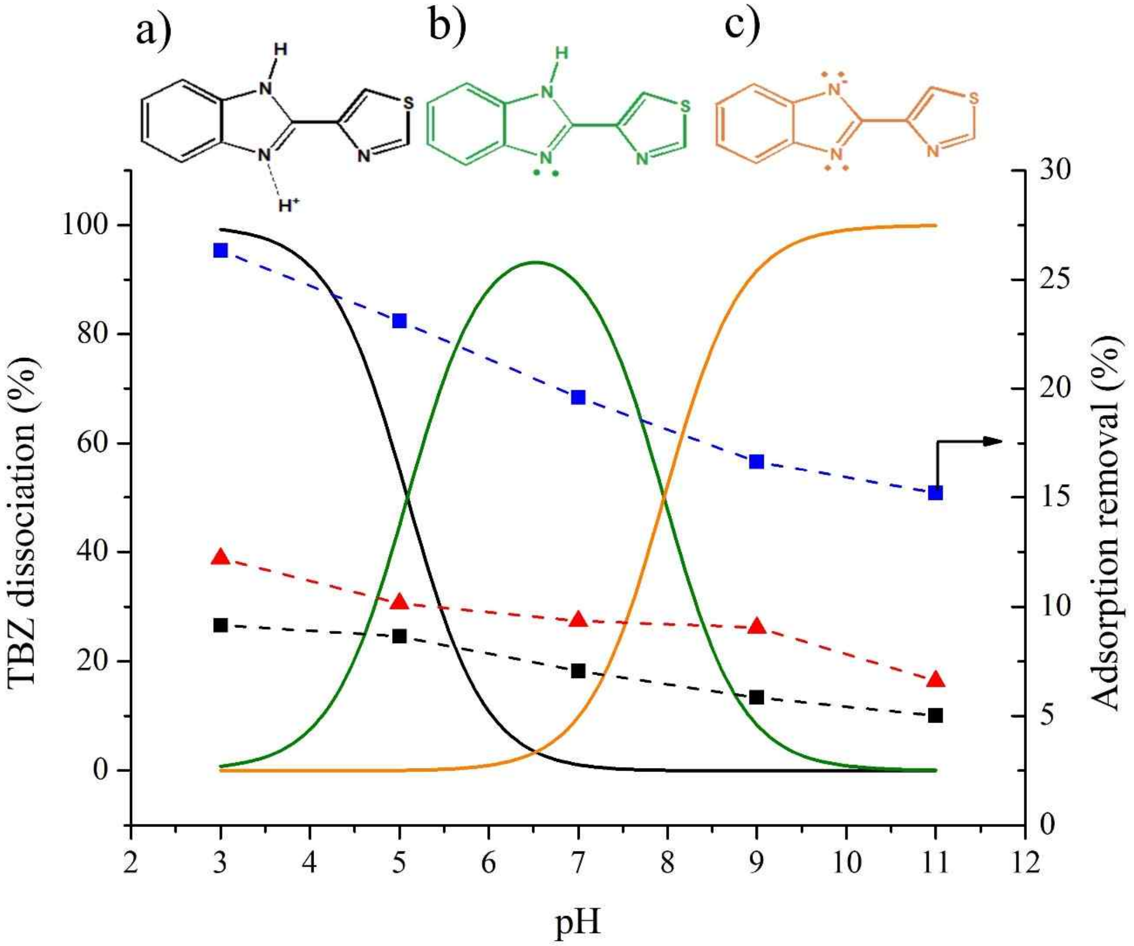

Figure 11. TBZ dissociation (positive specimen —, neutral specimen —, negative specimen —) and adsorption removal on (▲) C-ZnO, (■) T500, and (■) TPO-ZnO versus pH. Initial TBZ concentration 10 mg/L, ZnO 500 mg/L, $pK_{a,1}$ 5.09, and $pK_{a,2}$ 7.96.

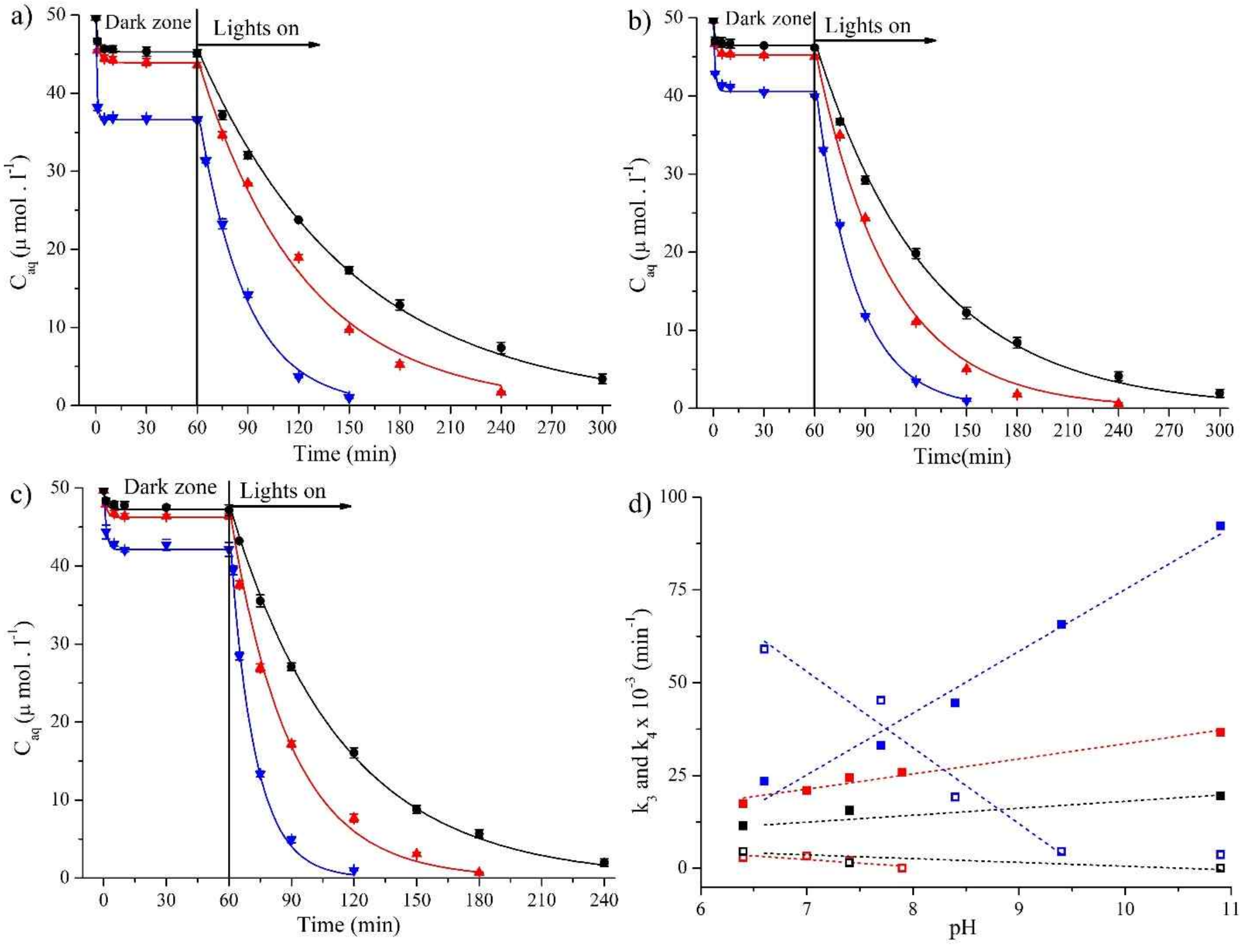

Figure 12. Effect of pH on TBZ adsorption and photocatalytic degradation removal. Dots are experimental data and continuous lines are calculated data by the model. a) pH 3, b) pH 7, c) pH 11. C-ZnO (▲), T500 (▼), TPO-ZnO (●) d) k_3 and k_4 values, C-ZnO k_3 (■), T500 k_3 (■), TPO-ZnO k_3 (■), C-ZnO k_4 (□), T500 k_4 (□), TPO-ZnO k_4 (□). TBZ 10 mg/L, and ZnO 500 mg/L.

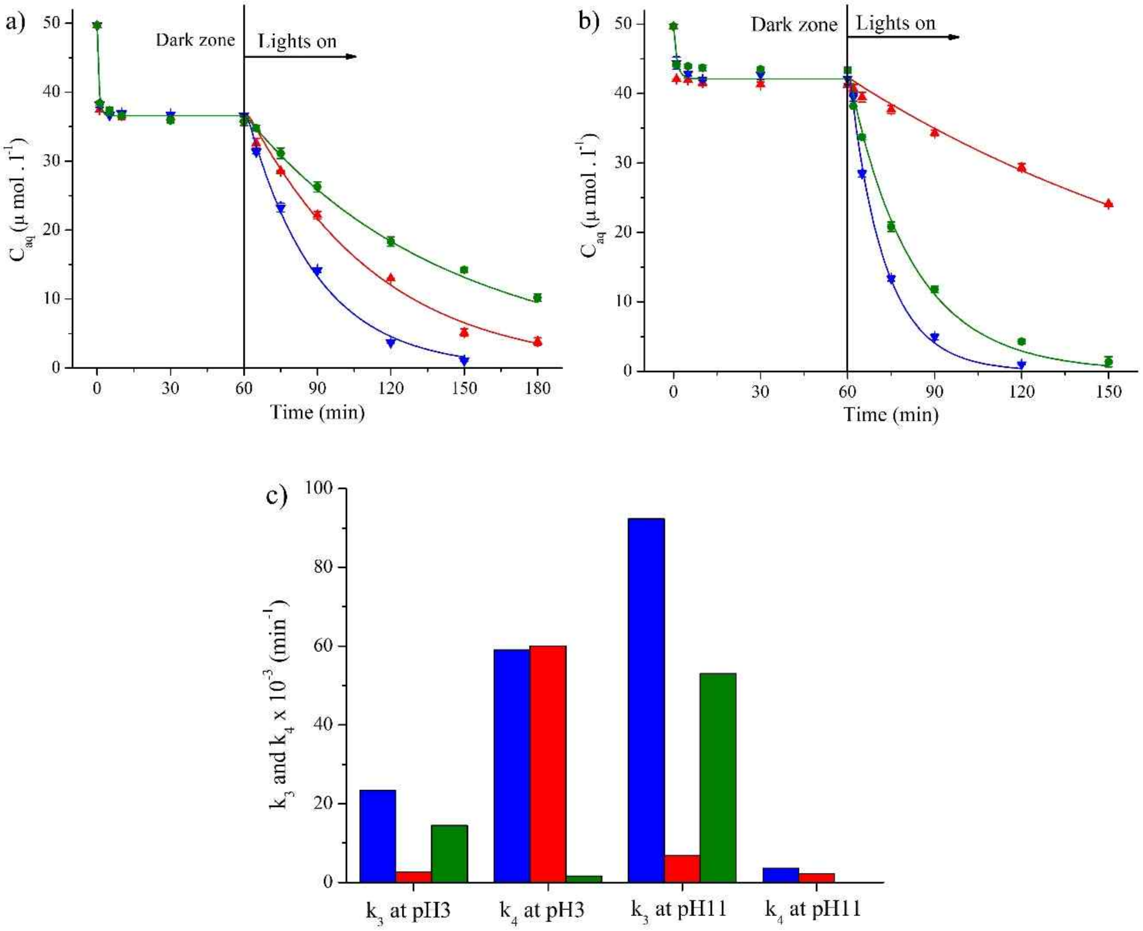

Figure 13. Effect of hydroxyl radical scavengers (▲), and hole scavengers (●) comparing to experiment without scavengers (▼) with T500 catalyst at a) pH 3 and b) pH 11. c) k_3 and k_4 at experiments without scavenger (■), with hydroxyl radical scavenger (■), and with hole scavenger (■). TBZ 10 mg/L, and T500 catalyst 500 mg/L.

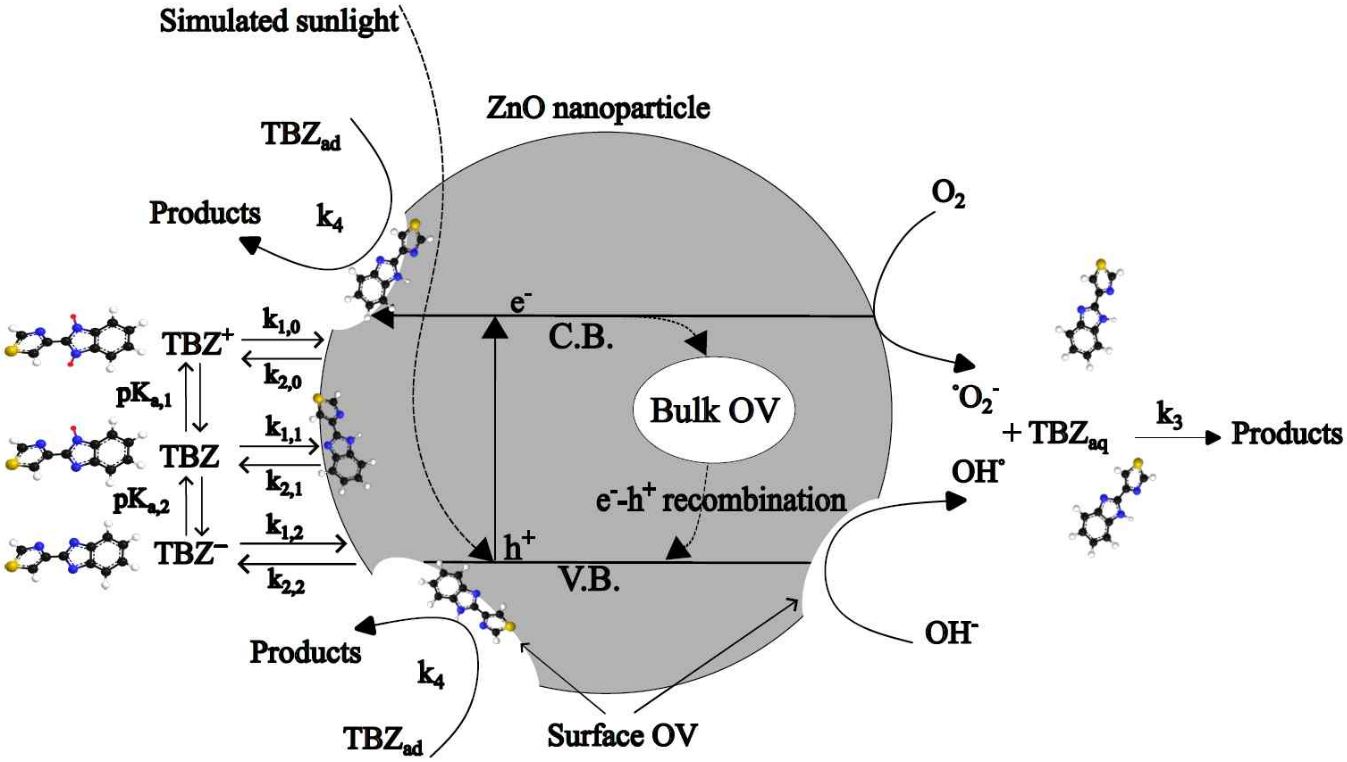

Figure 14. Proposed reaction mechanism for TBZ degradation at catalyst surface and in the solution.

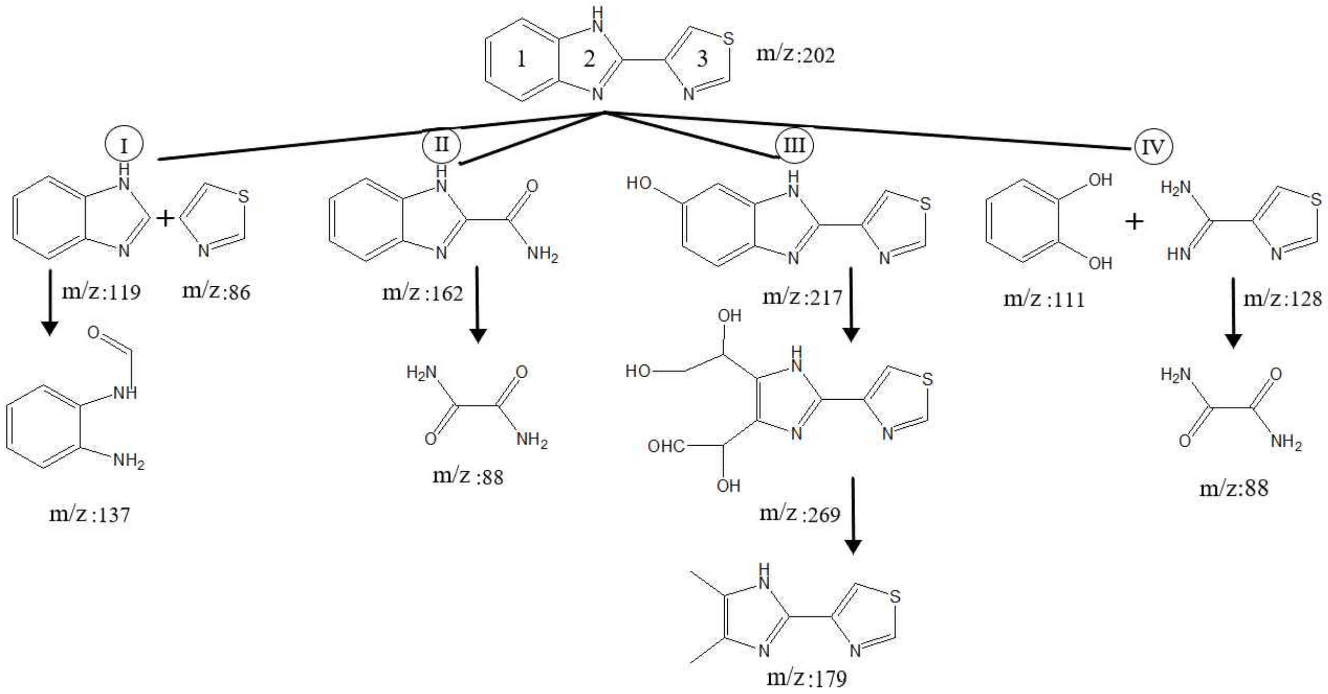

Figure 15. Degradation pathway and possible products of TBZ by T500 catalyst. Initial TBZ concentration 20 mg/L, T500 500 mg/L, pH7.

Table 1. Summary of reduction and pH conditions for the treatment of ZnO catalysts. All experiments are performed in duplicate and the error bars are demonstrated in the corresponding figures. TBZ initial concentration is 10 mg/L, catalyst concentration 500 mg/L, light intensity 1700 W/m^2, and the volume of solution is 50 mL for all experiments.

Experiment	Catalyst (reduction temperature)	Reduction time (hr)	Initial pH	Figure
1	C-ZnO	0	7	(2) and (12)
2	T270	5	7	(2)
3	T415	5	7	(2)
4	T470	5	7	(2)
5	T500	5	7	(2) and (12)
6	T650	5	7	(2)
7	T500	1	7	(2)
8	T500	3	7	(2)
9	T500	7	7	(2)
10	T500	5	3	(12) and (S.11)
11	T500	5	5	(S.11) and (S.12)
12	T500	5	7	(12) and (S.11)
13	T500	5	9	(S.11) and (S.12)
14	T500	5	11	(12) and (S.11)
15	C-ZnO	0	3	(12) and (S.11)
16	C-ZnO	0	5	(S.11) and (S.12)
17	C-ZnO	0	7	(12) and (S.11)
18	C-ZnO	0	9	(S.11) and (S.12)
19	C-ZnO	0	11	(12) and (S.11)
20	TPO-ZnO	5 (Oxidation)	3	(12)
21	TPO-ZnO	5 (Oxidation)	7	(12)
22	TPO-ZnO	5 (Oxidation)	11	(12)
23	T500	5	3 with IPA scavenger	(13)
24	T500	5	11 with IPA scavenger	(13)

25	T500	5	3 with KI scavenger	(13)
26	T500	5	11 with KI scavenger	(13)
27 (reuse)	T500	5	7	(S.18)

Table 2: EDS analysis results for different catalysts. [1]

	Sample	O (wt%)	Zn (wt%)	x (ZnO_{1-x})	Mass loss (mg)
1	C-ZnO	24.99	75.01	0.00	-
2	T270	23.54	76.46	0.03	6.2
3	T415	22.84	77.16	0.05	9.8
4	T470	21.95	78.05	0.07	12.4
5	T500	20.84	79.16	0.10	18.1
6	T650	20.81	79.19	0.10	52.8

[1] Initial mass of each sample is 200 mg. The mass loss is measured by the difference between the mass of each sample before and after reduction.

Table 3: Estimated crystalline size (D) and lattice strain (ε) of ZnO samples.

	Sample	D (Scherrer)	D (Williamson-Hall)	ε (Williamson-Hall)
1	C-ZnO	5.3±0.4	6.2±0.8	27.5×10^{-4}
2	T500	5.4±0.3	6.0±0.5	17.0×10^{-4}
3	T650	6.9 ±0.6	6.8±1.0	6.91×10^{-5}

Table 4: Estimated parameters of the kinetic model for TBZ adsorption and degradation on C-ZnO and T500.

	Parameter	C-ZnO	T500	TPO-ZnO
1	$k_{1,0}$ (g mol^{-1} min^{-1})	$1.68\ 10^{3}$	$4.04\ 10^{3}$	$1.59\ 10^{3}$
2	$k_{1,1}$ (g mol^{-1} min^{-1})	$4.63\ 10^{2}$	$9.66\ 10^{2}$	$4.15\ 10^{2}$
3	$k_{1,2}$ (g mol^{-1} min^{-1})	$3.26\ 10^{2}$	$4.50\ 10^{2}$	$2.51\ 10^{2}$
4	$k_{2,0}$ (g L^{-1} min^{-1})	$1.12\ 10^{-1}$	$1.69\ 10^{-1}$	$1.14\ 10^{-1}$
5	$k_{2,1}$ (g L^{-1} min^{-1})	$2.53\ 10^{-1}$	$2.10\ 10^{-1}$	$2.87\ 10^{-1}$
6	$k_{2,2}$ (g L^{-1} min^{-1})	$2.45\ 10^{-1}$	$2.07\ 10^{-1}$	$2.42\ 10^{-1}$
7	$K_{ad,0}$ (L mol^{-1})	$1.49\ 10^{4}$	$2.39\ 10^{4}$	$1.40\ 10^{4}$
8	$K_{ad,1}$ (L mol^{-1})	$1.83\ 10^{3}$	$4.59\ 10^{3}$	$1.45\ 10^{3}$
9	$K_{ad,2}$ (L mol^{-1})	$1.33\ 10^{3}$	$2.18\ 10^{3}$	$1.04\ 10^{3}$
10	k_3 (pH 3) (min^{-1})	$1.75\ 10^{-2}$	$2.34\ 10^{-2}$	$1.14\ 10^{-2}$
11	k_3 (pH 5) (min^{-1})	$2.10\ 10^{-2}$	$3.32\ 10^{-2}$	-
12	k_3 (pH 7) (min^{-1})	$2.45\ 10^{-2}$	$4.45\ 10^{-2}$	$1.56\ 10^{-2}$
13	k_3 (pH 9) (min^{-1})	$2.59\ 10^{-2}$	$6.58\ 10^{-2}$	-
14	k_3 (pH 11) (min^{-1})	$3.66\ 10^{-2}$	$9.23\ 10^{-2}$	$1.95\ 10^{-2}$
15	k_4 (pH 3) (min^{-1})	$2.88\ 10^{-3}$	$5.90\ 10^{-2}$	$4.51\ 10^{-3}$
16	k_4 (pH 5) (min^{-1})	$3.30\ 10^{-3}$	$4.53\ 10^{-2}$	-
17	k_4 (pH 7) (min^{-1})	$1.99\ 10^{-3}$	$1.92\ 10^{-2}$	$1.44\ 10^{-3}$
18	k_4 (pH 9) (min^{-1})	0	$4.53\ 10^{-3}$	-
19	k_4 (pH 11) (min^{-1})	0	$3.66\ 10^{-3}$	0

20	C_{tot} (mol g^{-1})	1.17 10^{-4}	1.96 10^{-4}	1.06 10^{-4}
21	m	1.12	2.09	1.06
22	pk_{a1}	5.09	5.09	5.09
23	pk_{a2}	7.96	7.96	7.96

Table 5: Comparison of the results of this study with similar photocatalytic degradation studies using OV catalysts.

Catalyst	Contaminant	OV production	Light source	Max k (min^{-1})	Ref.
ZnO	Rhodamine-B	Calcination	UV	0.042	[19]
Ag-ZnO/CeO_2	Methane	Photo deposition	SSL[1]	0.017	[44]
ZnO@In_2O_3	Tetracycline	Doping/calcination	SSL	0.010	[101]
Ag-ZnO	Methyl orange	Metal deposition	SSL	0.120	[102]
ZnO	Tetracycline	$NaBH_4$ reduction	SSL	0.062	[103]
ZnO	TBZ and MB	H_2 reduction	SSL	k_3 =0.092 k_4 =0.059	Present work

[1] Simulated sunlight